3 Radiative Properties of Opaque Materials

3.1 INTRODUCTION

Detailed radiation transfer predictions require knowledge of the spectral or total radiative properties of surfaces and the media between them. Some of these properties may be measured, although experimental conditions often depart from those of practical applications. As we discuss in Chapter 8, properties of optically smooth interfaces can be derived using electromagnetic (EM) wave theory. While it is usually inadequate to quantify the properties of real-world surfaces that are not perfectly clean and optically smooth, EM theory often yields useful trends and provides a unifying basis to help explain radiation phenomena. This chapter reports radiative properties of several opaque materials as a function of different parameters. It begins with a brief introduction to dielectric and electrically conducting materials. Examples of measured properties of real opaque materials are presented, along with comparisons with those obtained from EM theory predictions. Surface roughness and contamination can influence radiative properties, particularly the directional-spectral emissivity and reflectivity, and we introduce some theories to account for these effects. Finally, we demonstrate how radiative properties can be selected for important applications, notably those related to solar energy.

We will not make any attempt to provide comprehensive radiative property data in this text. However, a selective property table is given in Appendix B. Extensive tabulations and graphs of radiative properties are available in the literature, including Wood et al. (1964), Svet (1965), Touloukian and Ho (1970), Touloukian and DeWitt (1972a), Touloukian et al. (1972b), Henninger (1984), Palik (1998), Fox (2001), Seo et al. (2019, for cryogenic temperatures), and Rumble et al. (2018, 2019), as well as recent journal articles for particular materials.

3.2 ELECTROMAGNETIC WAVE THEORY PREDICTIONS

James Clark Maxwell (1864) provided the crowning achievement of classical physics that explained the relation between electric and magnetic fields. Maxwell's EM wave equations provide the required framework for obtaining the radiative properties of opaque materials and surfaces. For "optically smooth" surfaces, these equations can be used to obtain spectral-directional reflectivity, transmissivity, absorptivity, and emissivity from the optical and electrical properties of the bulk material. In this context, "optically smooth" means that surface imperfections, roughness, or texture are much smaller than the wavelength of the incident radiation to the extent that they do not affect the far-field wave-fronts, and wave/surface interactions are strictly *specular* (mirror-like) in nature. (The term specular must not be confused with *spectral*, which indicates a wavelength-specific attribute).

Maxwell's equations govern how EM waves behave at the interface between two media. These calculations require the complex index of refraction, $\bar{n} = n - ik$, which describes how the wave propagates through the medium, as discussed in Chapter 8. This quantity is always wavelength-dependent, although this notation is often excluded. It is sometimes convenient to instead work with the complex dielectric constant $\bar{\epsilon} = \epsilon_{\mathrm{I}} - i\epsilon_{\mathrm{II}}$. These quantities are related by

and

The departures of real surfaces from the ideal conditions assumed in theoretical predictions (e.g., due to roughness and contamination) often result in large differences between modeled and measured properties. Despite these limitations, EM theory provides an understanding of why there are basic differences in the radiative properties of insulators and electrical conductors and reveals general trends that help unify presentation of experimental data. As discussed in Chapter 8, EM wave theory also explains the angular dependence of directional reflectivity, absorptivity, and emissivity for smooth surfaces. Finally, since the theory applies to pure substances with ideally smooth surfaces, it also provides a means for computing a limit of attainable properties, such as maximum reflectivity or minimum emissivity of a metallic surface.

3.2.1 Dielectric Materials

3.2.1.1 Reflection and Refraction at the Interface between Two Perfect Dielectrics (No Wave Attenuation, $k \to 0$)

A medium is a perfect dielectric if it does not absorb incident radiation. Then, the complex index of refraction of a dielectric medium is expressed only with its real component n, as k is zero. The imaginary term of the complex dielectric constant is also equal to zero, so $\bar{\epsilon} = \epsilon_{\mathrm{I}} = \epsilon$. While this is an idealization, it is quite a good approximation for many interfaces, such as air–water or air–glass interfaces for the visible spectrum, but *only in the portion of spectrum where* $k = 0$. For example, window glass behaves as a perfect dielectric over visible wavelengths; in the near-infrared spectrum (beyond approximately 2.2 μm, as discussed in Section 9.7), windows are opaque.

Consider an EM wave traveling through a dielectric medium with refractive index n_1, which encounters the smooth planar interface of a second medium with a refractive index n_2. If the angle of the incidence onto the surface of medium 2 is θ_i, then the wave is refracted into medium 2 at angle χ. The angle of incidence of θ_i, reflection θ_r, and refraction χ, which are all in the same plane (Figure 3.1), are related through Snell's law

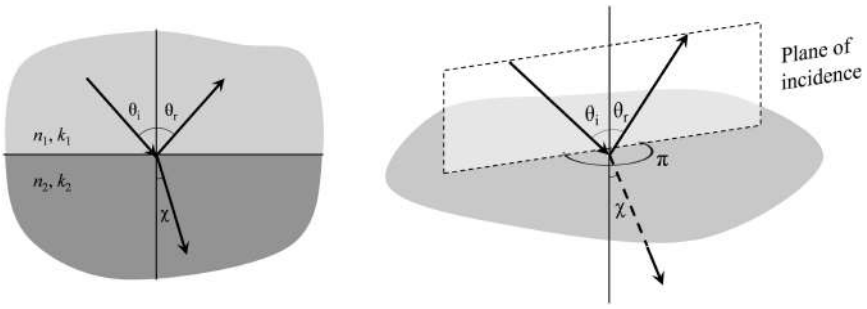

FIGURE 3.1 Geometric quantities for an EM wave at an interface between media 1 and 2.

which results in

The angle of reflection of an EM wave from an ideal interface is thus equal to its angle of incidence rotated about the normal to the interface through a circumferential angle of $\theta = \pi$. Equation (3.3) can be rearranged into

The energy carried by a wave is due to variation in both the electric field, *E*, and the magnetic field, *H*, which, according to Maxwell's equations, fluctuate in mutually orthogonal directions. The relative amplitudes of these fluctuations depend on the electrical permeability and magnetic permittivity of the medium through which the wave propagates. The energy of the propagating wave is proportional to the product of the amplitudes of these fluctuations, or, since *H* is proportional to *E*, to the square of the wave amplitude of *E* (or *H*, for that matter), and is properly expressed as the Poynting vector. Squaring the amplitude ratio of reflected to incident amplitude gives the ratio of energy reflected from a surface to energy incident from a given direction.

We can also resolve the electric and magnetic fields into orthogonal *polarization* components which sum to the total intensity. It is convenient to define the polarization components relative to the plane of incidence and the oscillating plane of the electric field. The perpendicular and parallel components oscillate perpendicular and parallel to the incidence plane, respectively, and both are perpendicular to the direction of the propagation.

3.2.1.2 Reflectivity

The specular reflectivity of a wave incident on a surface at angle θ and polarized parallel or perpendicular to the plane of incidence is obtained from

and

The subscript λ is a consequence of the fact that the refractive indices used to calculate χ depend on wavelength.

Useful forms containing only θ_i are obtained by eliminating χ in Equations (3.6) and (3.7) using Equation (3.5):

The parallel reflectance component equals zero when $\theta_i = \tan^{-1}(n_2/n_1)$, which is called *Brewster's* angle. Radiation reflected at this angle is all perpendicularly polarized.

The reflectivity for unpolarized incident radiation is given by the Fresnel equation (see Chapter 8)

The average of Equations (3.8) and (3.9) is often used to obtain the angular reflectivity profile $\rho_\lambda(\theta_i)$ in terms of θ_i only. For normal incidence, $\theta_i = 0$, and the reflectivity becomes

Electromagnetic theory requires the interface to be perfectly clean and optically smooth. These conditions are typically satisfied for lenses, windows, and other optical components, and therefore the optical components can be accurately modeled using the Fresnel equations for most wavelengths of interest. Predictions of the normal reflectivity from the EM theory for various dielectrics are listed in Table 3.1. Note that for most cases of interest we can take $n_1 = 1$ (e.g., for incidence in air or a vacuum). Also, these relations are for an interface on an opaque material, so there is no reflection from a second internal surface in medium 2. The cases of nonopaque layers (e.g., windows and glazings) are considered in Chapter 17.

TABLE 3.1

Optical Property Values and Normal Spectral Reflectivity of Various Dielectric Materials at T = 300 K and λ =0.589 μm

Material	n (Refractive Index)	$\epsilon = \gamma/\gamma_0$ (Dielectric constant)	$\rho_{\lambda,n}$ Equation (3.11)
SiO_2 (glass)	1.458	4.42	0.035
SiO_2 (fused quartz)	1.544	3.75	0.046
NaCl	1.5441	5.90	0.046
KCl	1.4902	4.86	0.039
H_2O (liquid)	1.332	77.78	0.020
H_2O (ice, 0°C)	1.309	91.60	0.018
Vacuum	1	1	0.000

Source: Lide, D. R. (ed.) *Handbook of Chemistry and Physics*, 88th Ed., CRC Press, Boca Raton FL, 2008.

3.2.1.3 Emissivity

One can obtain the directional emissivity from the directional reflectivity according to Kirchhoff's law, as we discuss in Chapter 2. For a nontransparent (opaque) medium, we can write

since emission is always unpolarized. As is the case for directional reflectivity, directional emissivity also depends on the index of refraction of the emitting body and the surrounding medium. Figure 3.2 shows different curves for various n_2/n_1, where $n_2 > n_1$. When $n_2 < n_1$, there is a limiting angle such that radiation at larger incidence angles is totally reflected (*total internal reflection*); this is discussed in Section 17.5.2. When $\rho(\theta)$ is computed for incident radiation in air ($n_1 \approx 1$), the ratio n_2/n_1 reduces to the refractive index of the material on which the radiation is incident. Figure 3.2 gives the emissivity of a dielectric into air when n_2/n_1 in the figure is set equal to the simple refractive index n of the emitting dielectric. For $(n_2/n_1) = 1$, the emissivity is one (blackbody case), and the curve in Figure 3.2 is circular with a radius of one.

As (n_2/n_1) increases, the curves remain approximately circular up to about $\theta = 70°$ and then decrease rapidly to zero at $\theta = 90°$. Thus, dielectric materials emit poorly at large angles from the normal direction. The emissivity is large for angles less than 70°, so that, in a hemispherical sense, dielectrics are good emitters. The assumptions used in applying Maxwell equations restrict these findings to wavelengths longer than the visible spectrum, as verified by comparisons with experimental measurements.

From the directional-spectral emissivity, the hemispherical-spectral emissivity can be computed from Equation (2.7) as $\varepsilon_\lambda(T) = (1/\pi)\int_\cap \varepsilon_\lambda(T,\theta,\phi)\cos\theta d\Omega$. Then an integration can be performed over all wavelengths to obtain the hemispherical total emissivity as in Equation (2.8).

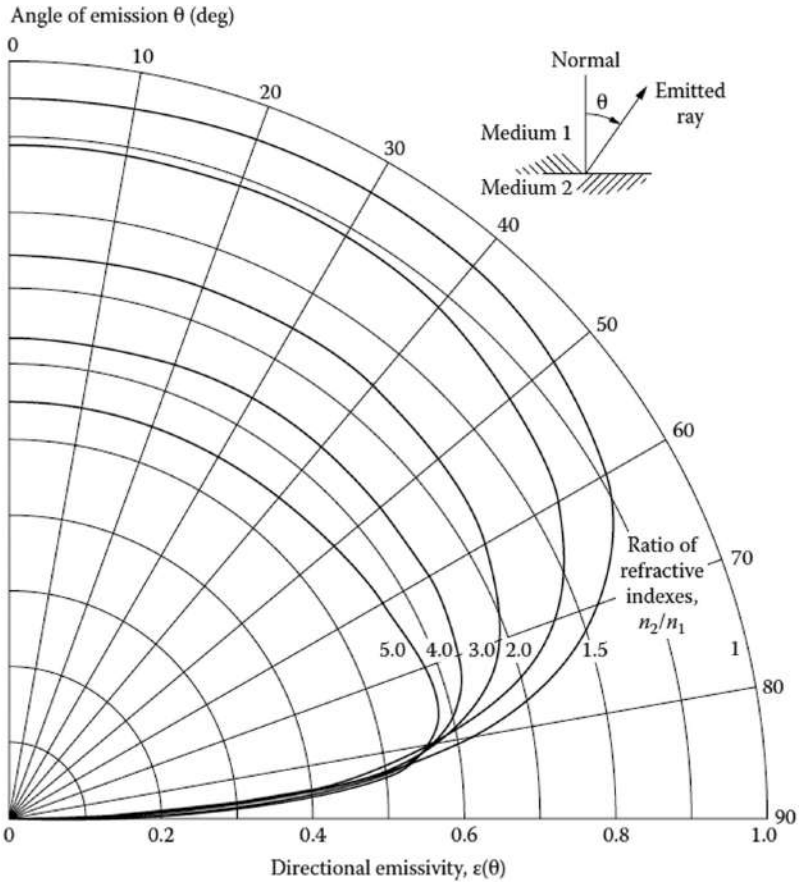

FIGURE 3.2 Directional emissivity predicted from EM theory.

The integration of $\varepsilon_\lambda(\theta)$ over all directions to evaluate the hemispherical ε_λ is complicated, but the integration has been carried out to yield ε in terms of n_2/n_1:

The normal emissivity is a convenient value to which the hemispherical value may be compared:

This parameter is shown as a function of n_2/n_1 in Figure 3.3a. Note that normal emissivities of less than about 0.50 correspond to $n_2/n_1 > 6$. Such large n_2/n_1 values are uncommon for dielectrics, so the curve is not extended to smaller ε_n. The hemispherical emissivity for dielectrics is compared to the normal value in Figure 3.3b.

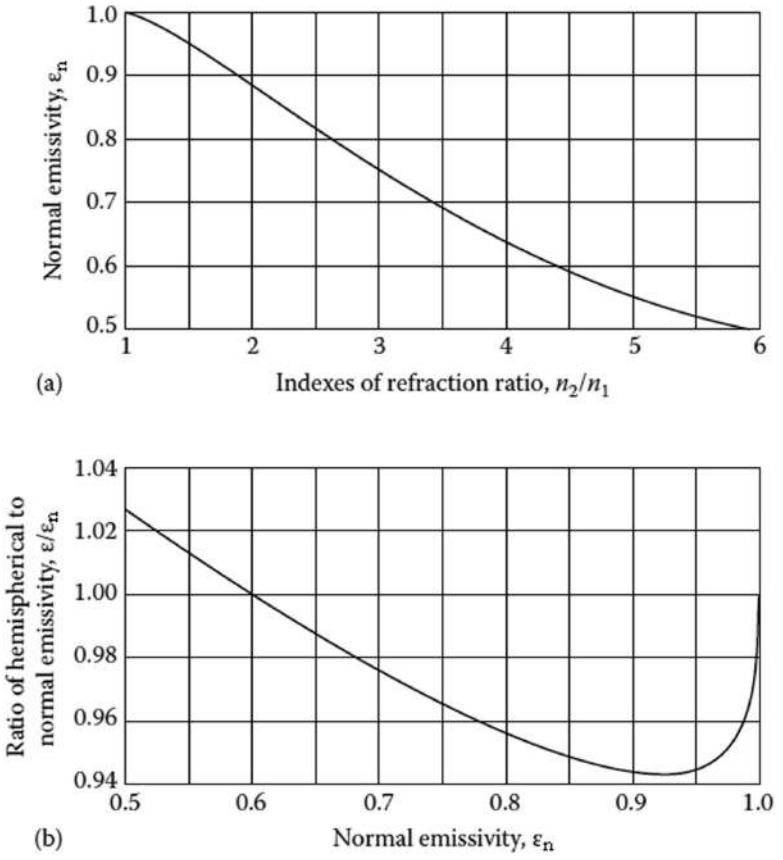

FIGURE 3.3 Predicted emissivities of dielectric materials for emission into a medium with a refractive index n_1 from a medium with a refractive index n_2 where $n_2 \geq n_1$. (a) Normal emissivity as a function of n_2/n_1, and (b) comparison of hemispherical and normal emissivity.

For large n_2/n_1, the ε_n values are relatively low, and with increasing n_2/n_1, the curves in Figure 3.2 depart more from a circular form. Figure 3.3b reveals that the flattening of the curves of Figure 3.2 in the region near the normal causes the hemispherical emissivity to exceed the normal value at large n_2/n_1 ($\varepsilon_{\lambda,n} \approx 0.5-0.6$). For n_2/n_1 near 1 ($\varepsilon_{\lambda,n}$ near 1), the hemispherical ε_λ is lower than $\varepsilon_{\lambda,n}$ because of poor emission at large θ.

3.2.2 Radiative Properties of Conductors

3.2.2.1 Electromagnetic Relations for Incidence on an Absorbing Medium

In the preceding section, we discussed perfect dielectrics where there is no attenuation ($k=0$) of radiation as it travels within the material. In other words, we assumed that the material is perfectly

transparent except for interface reflections. For real dielectrics, there is attenuation, so k is nonzero, although it is small.

The propagation of an EM wave within an attenuating medium is governed by the same relations as a nonattenuating medium if the refractive index n is replaced by the complex index, $\bar{n} = n - ik$, although this leads to some complexities in interpretation, particularly at the interface between media. For example, in the case of an EM wave within a dielectric medium (n_1) incident upon a conducting medium ($\bar{n}_2 = n_2 - ik_2$), Equation (3.5) becomes

Consequently, sin χ is complex, and χ can no longer be interpreted as the angle of refraction for propagation into the material because the transmitted wave is *heterogeneous* (*cf.* Section 8.4.2). Also, except for normal incidence, n_2 is not directly related to the wave propagation velocity.

The equations for the reflected components of incident radiation are also more complicated than the case of two dielectrics. One of the earlier analyses was provided by Hering and Smith (1968) who gave the following form for incidence from air or vacuum ($n_1 = 1$, $k_1 = 0$, $n_2 = n$, $k_2 = k$):

where

and

The reflectance at normal incidence reduces to

The directional emissivity can be found from Kirchhoff's law, $\varepsilon_\lambda(\theta) = 1 - [\rho_{\lambda,\perp}(\theta) + \rho_{\lambda,\parallel}(\theta)]/2$, which can then be integrated over the hemisphere to obtain the hemispherical emissivity, $\varepsilon_\lambda = \int_0^1 \varepsilon_\lambda(\theta)\, d(\sin^2\theta)$, as a function of n and k. One set of results, for $n \geq 1$, is plotted in Figure 3.4 as a function of n and k/n, which shows how the hemispherical emittance decreases as both n and k increase.

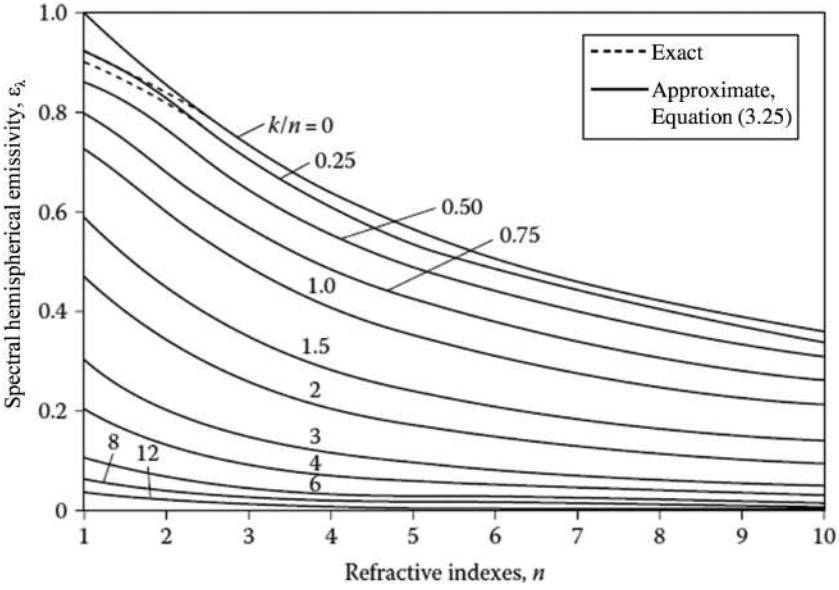

FIGURE 3.4 Exact and approximate hemispherical emissivity results ($n \geq 1.0$). (From Hering, R.G. and Smith, T.F., *IJHMT*, 11(10), 1567, 1968).

These results apply for radiation incident from air or a vacuum, with $n_1 \approx 1$. Harpole (1980) presented an analysis for the more complex case of oblique incidence from an adjacent absorbing material.

3.2.2.2 Reflectivity and Emissivity Relations for Metals (Large *k*)

Usually conductors (such as metals) are internally highly absorbing; this means that the extinction coefficient k is sufficiently large to simplify the above equations into more convenient results. For large k, the $\sin^2\theta$ terms in Equations (3.18) and (3.19) can be neglected relative to n^2+k^2. Then $\alpha \approx \beta \approx \gamma \approx 1$ and Equations (3.16) and (3.17) yield

and

For unpolarized incident radiation, $\rho(\theta_i) = [\rho_{\parallel}(\theta_i) + \rho_{\perp}(\theta_i)]/2$, and for the normal direction, ρ_n reduces to Equation (3.21). Emission is unpolarized, so the directional emissivity is given by Equation (3.12). In the normal direction ($\theta_i = 0$), this becomes

These emissivity relations are demonstrated in Figure 3.5 for a pure smooth platinum surface at a wavelength of 2 μm, and in Figure 3.6 for a titanium surface at multiple wavelengths. For metals,

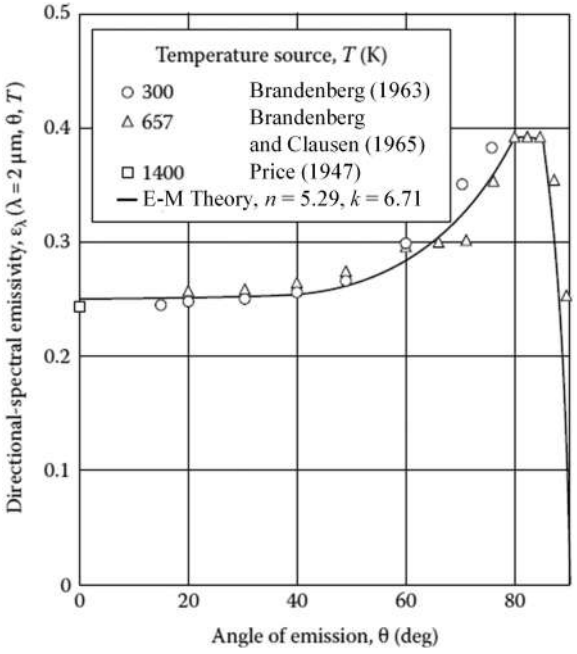

FIGURE 3.5 Directional-spectral emissivity of platinum at $\lambda = 2$ μm. Refractive indices are from Lide (2008).

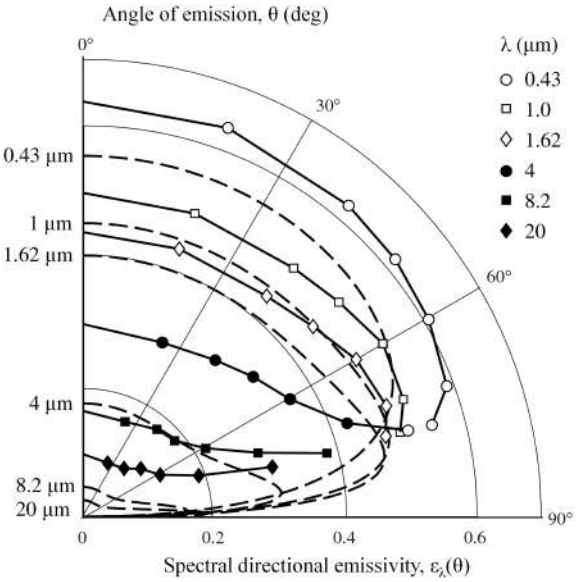

FIGURE 3.6 Directional-spectral emissivity of titanium at 306 ± 14 K. Surface ground to 0.4 μm rms roughness. Symbols denote data from Edwards, D. K., and Catton, I.: Radiation characteristics of rough and oxidized metals, in S. Gratch (ed.) *Advances in Thermophysical Properties at Extreme Temperatures and Pressures*, pp. 189–199, ASME, New York, 1964. Dashed curves are predictions from EM theory using optical constants in Palik, E. D. (ed.) *Handbook of Optical Constants of Solids*, Elsevier, New York, 1998.

the emissivity is essentially constant for $\theta_i < 50°$ away from the normal and then increases to a maximum within a few degrees of the tangent to the surface. It is evident by comparison with this and other experimental data from Harrison et al. (1961), Brandenberg (1963), Brandenberg and Clausen (1965), Price (1947), Palik (1998), and Rumble et al. (2018, 2019) that the general shape of the curve predicted by substituting Equations (3.22) and (3.23) into (3.12) is correct. This angular dependence of emissivity for metallic surfaces contrasts with the behavior of dielectrics, for which emissivity decreases substantially as the angle from the normal becomes larger than about 70°.

Normal spectral reflectivities calculated using Equation (3.24) are shown in Table 3.2. A wavelength of $\lambda = 0.484$ μm is in the visible range, close to the short-wavelength region where the EM theory becomes inaccurate.

The values in Table 3.2 predicted by Equation (3.21) agree with measured $\varepsilon_{\lambda,n}$ at $\lambda = 8$ μm (0.1 eV), but are in greater error at $\lambda = 0.484$ μm (2.4 eV). For the cases of poor agreement, it is difficult to ascribe the error specifically to the optical constants, to the measured emissivity, or to the theory itself, although the theory is expected to be less accurate at shorter wavelengths. Most probably the optical constants are somewhat in error, and the experimental samples do not meet the standards of perfection in surface preparation demanded by the theory.

TABLE 3.2
Optical Properties and Normal Spectral Reflectivity of Metals at $T = 298$ K and $\lambda = 0.484$ μm and 8.06 μm

Material (electrical resistivity, r_e [$\times 10^6$ (Ω·cm)])	Wavelength, λ (μm)	Refractive index, n	Absorption index, k	Normal Spectral Reflectivity, $\rho_{\lambda,n}$	
				Eq. (3.24)	Eq. (3.29)
Aluminum	0.484	0.826	6.283	0.923	0.883
(2.709)	8.06	34.464	105.6	0.989	0.970
Chromium	0.484	2.75	4.46	0.676	0.826
(12.6)	8.06	11.81	29.76	0.955	0.955
Copper	0.484	1.12	2.60	0.602	0.933
(1.712)	8.06	29.69	71.57	0.980	0.983
Gold	0.484	0.50	1.86	0.650	0.924
(2.255)	8.06	8.17	82.83	0.995	0.981
Iron	0.484	2.56	3.31	0.567	0.845
(9.87)	8.06	6.41	33.07	0.978	0.960
Nickel	0.484	1.71	3.06	0.591	0.867
(7.12)	8.06	9.54	45.82	0.983	0.966
Platinum	0.484	2.03	3.54	0.626	0.839
(10.7)	8.06	13.21	44.72	0.976	0.959
Titanium	0.484	1.81	2.47	0.483	0.71
(39)	8.06	5.03	23.38	0.965	0.92
Tungsten	0.484	3.45	2.72	0.493	0.883
(5.39)	8.06	14.06	54.7	0.983	0.970

Source: Rumble, J. R. (ed.): *Handbook of Chemistry and Physics*, 100th Ed., CRC Press, Boca Raton FL, 2019.

Within the approximation of neglecting $\sin^2\theta_i$ relative to n^2+k^2, the hemispherical spectral emissivity for a metal in air or vacuum is found by substituting the directional spectral emissivity found from Equations (3.22) and (3.23) into Equation (2.7). Integrating gives

Without neglecting $\sin^2\theta$, the hemispherical ε_λ was calculated by numerical integration, as shown in Figure 3.4, and the results were compared with those from Equation (3.25) for various n and k values. They found that for the accuracy of Equation (3.25) to be within 1%, 2%, 5%, or 10% of the numerically integrated values, n^2+k^2 should be larger than 40, 3.25, 1.75, and 1.25, respectively. Based on the optical constants given in Table 3.2, Equation (3.25) should usually be accurate for most metals, within a few percent.

From Equation (3.24), the normal emissivity of both metals and attenuating dielectrics into air can be computed as a function of n and k. This is shown in Figure 3.7, and more complete results

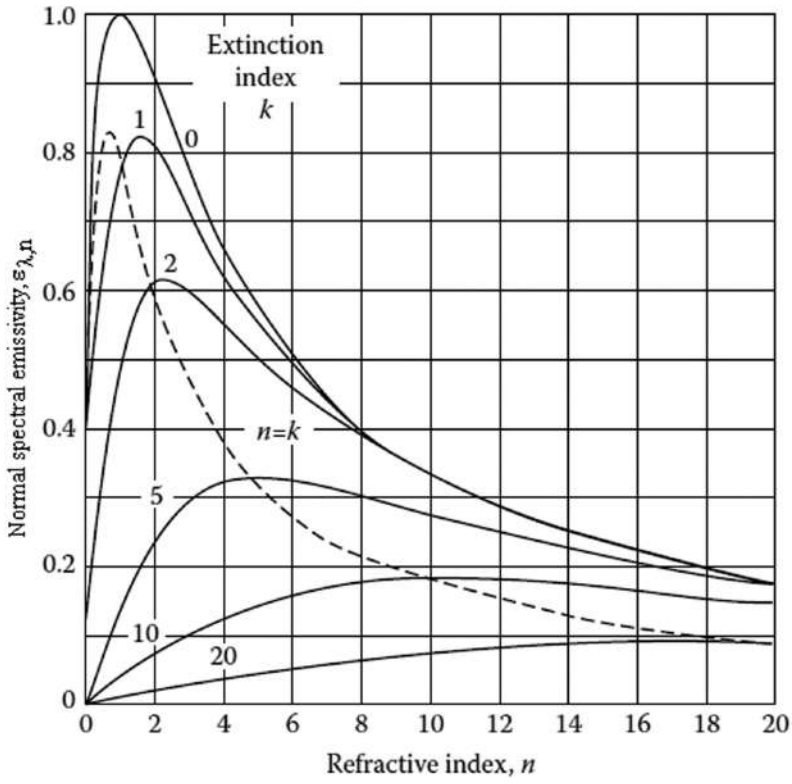

FIGURE 3.7 Emissivity of attenuating medium emitting into air.

are provided by Hering and Smith (1968). For polished metals, when $\varepsilon_{\lambda,n}$ is less than about 0.5, the hemispherical emissivity is usually larger than the normal value because of the increase in emissivity in the tangential direction, as shown in Figures 3.5 and 3.6. Hence, in a table listing emissivity values for polished metals, if $\varepsilon_{\lambda,n}$ is given, it should be multiplied by a factor larger than unity, such as is obtained by comparing Equations (3.24) and (3.25). In the visible wavelength region, $\varepsilon_\lambda/\varepsilon_{\lambda,n}$ is close to 1, but in the infrared (IR), some values approach 1.2. Surfaces that are not optically smooth and may be contaminated (e.g., by an oxide) tend to be more diffuse than for polished specimens.

3.2.2.3 Relations between Radiative Emission and Electrical Properties

The wave solutions to Maxwell's equations provide a means for determining n and k from the electric and magnetic properties of a material. For highly conducting metals (electrical resistivity, r_e, is small) and for relatively long wavelengths, $\lambda_0 > \sim 5$ μm

where μ_0 is the magnetic permeability, which for most metals can be taken to be the vacuum value. This is the *Hagen–Rubens equation* (Hagen and Rubens 1900). Predictions of n and k from this equation can be greatly in error, particularly at short wavelengths, as shown in Table 3.2. The restrictions of this equation to wavelengths greater than approximately 5 μm should be carefully noted.

With the conditions in Equation (3.26) that $n = k$, Equation (3.24) reduces to

for a material with refractive index n radiating in the normal direction into air or vacuum: Substituting Equation (3.26) into Equation (3.27) and expanding into a series gives the *Hagen–Rubens emissivity relation*:

Because the index of refraction of metals as predicted from Equation (3.26) is generally large at longer wavelengths so that (r_e/λ_o) is small, that is, for $\lambda > \sim 5$ μm (see Table 3.2), one or two terms of the series are usually adequate. A two-term approximation is made by adjusting the coefficients of the second term for the remaining terms in the series to yield

Data for polished nickel are shown in Figure 3.8, and the extrapolation to long wavelengths by Equations (3.29) is reasonable. The predictions of normal spectral reflectivity at long wavelengths ($\rho_{\lambda,n} = 1 - \varepsilon_{\lambda,n}$), as presented in Table 3.2, are much better than the predictions of the optical constants.

The angular behavior of the spectral emissivity can be obtained by substituting the refractive index, Equation (3.26), into Fresnel's relations, Equations (3.22) and (3.23), and this result into Kirchhoff's law, Equation (3.12), to yield the spectral directional emissivity, $\varepsilon_\lambda(\theta)$. Figure 3.6 shows

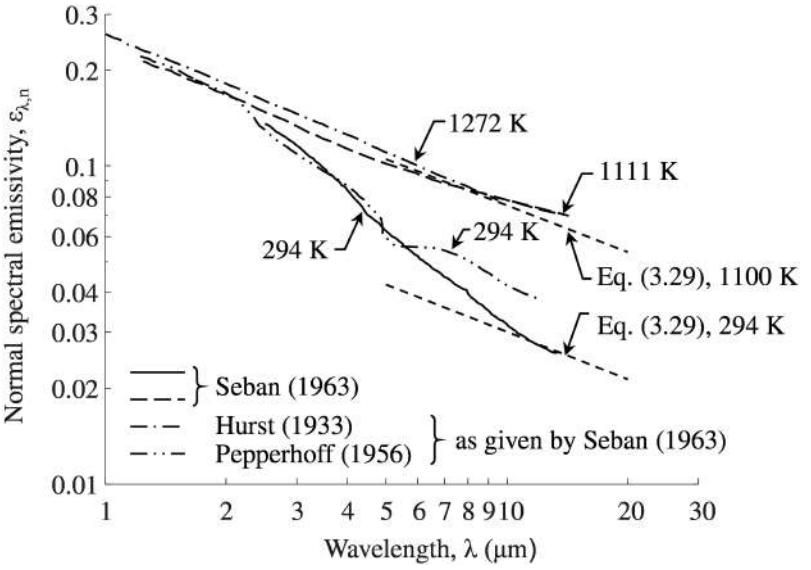

FIGURE 3.8 Comparison of measured values with theoretical predictions for normal spectral emissivity of polished nickel. Hagen–Rubens predictions are calculated using electrical resistivity from Chu, T. K., and Ho, C. Y., *Electrical Resistivity of Chromium, Cobalt, Iron, and Nickel* (CINDAS Report 60), Thermophysical Properties Research Centre, 1982.

that the directional spectral emissivity of titanium tends to decay with increasing wavelength, in accordance with Hagen–Rubens theory.

The normal spectral emissivity in Equation (3.28) can be integrated with respect to wavelength to yield a normal total emissivity, $\varepsilon_n(T) = \pi \int_0^\infty \varepsilon_{\lambda,n}(T) I_{\lambda b}(T)\, d\lambda / \sigma T^4$. Note that Equation (3.28) is accurate only for $\lambda_0 > \sim 5$ μm, so in performing the integration starting from a small value of λ (e.g., in the visible spectrum) assumes that the energy radiated at wavelengths shorter than 5 μm is assumed to be small compared with that at wavelengths longer than 5 μm. Then, substituting into the integral, the first term of Equations (3.28) and (1.20) for $I_{\lambda b}$ provides

where $\zeta = C_2/\lambda_0 T$, as was used in conjunction with Equation (1.39). The integration is carried out by use of gamma functions to yield

If additional terms in the series Equation (3.28) are retained, the recommended three-term approximation for total normal emissivity of a metal is obtained (Parker and Abbott 1964)

For pure metals, r_e near room temperature is approximately described by

where $r_{e,273}$ is the electrical resistivity at 273 K. Substituting Equation (3.33) into Equation (3.31) gives the approximate result

This indicates that the total emissivity of pure metals increases directly with absolute temperature. This expression was originally derived by Aschkinass (1905). In some cases, it holds to unexpectedly high temperatures where considerable emitted radiation is in the short-wavelength region (for platinum, to near 1800 K), but often it applies only to temperatures below about 550 K. This is illustrated in Figure 3.9 for platinum and tungsten (data from Lide 2008). In Figure 3.10, the normal emissivity for various polished surfaces of pure metals is compared with predictions based on Equation (3.34). The experimental data are obtained from three standard compilations (Hottel 1954, Eckert and Drake 1959, Lide 2008).

Likewise, the spectral directional emissivity found from the refractive index, Equation (3.26), and the Fresnel relations, Equations (3.22) and (3.23) can be integrated over all directions to obtain total hemispherical quantities. The following approximate equations for the hemispherical total emissivity fit the results in two ranges:

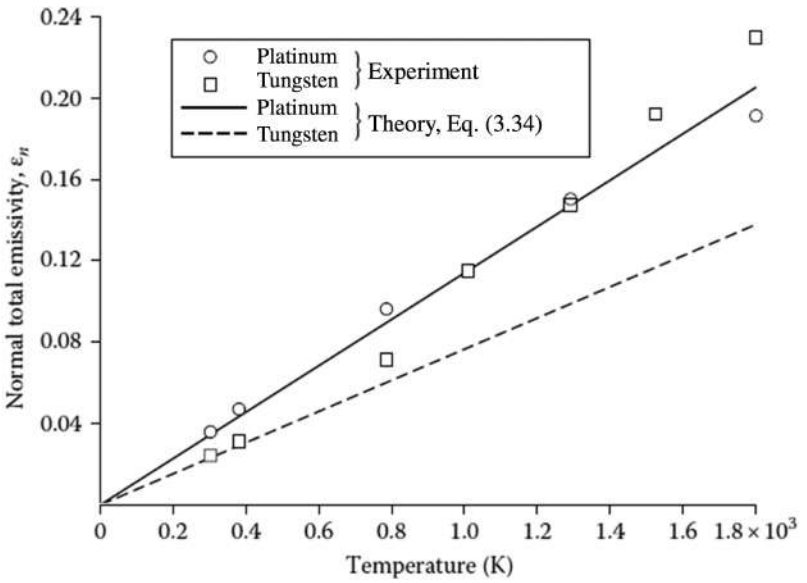

FIGURE 3.9 Temperature dependence of normal total emissivity of polished metals.

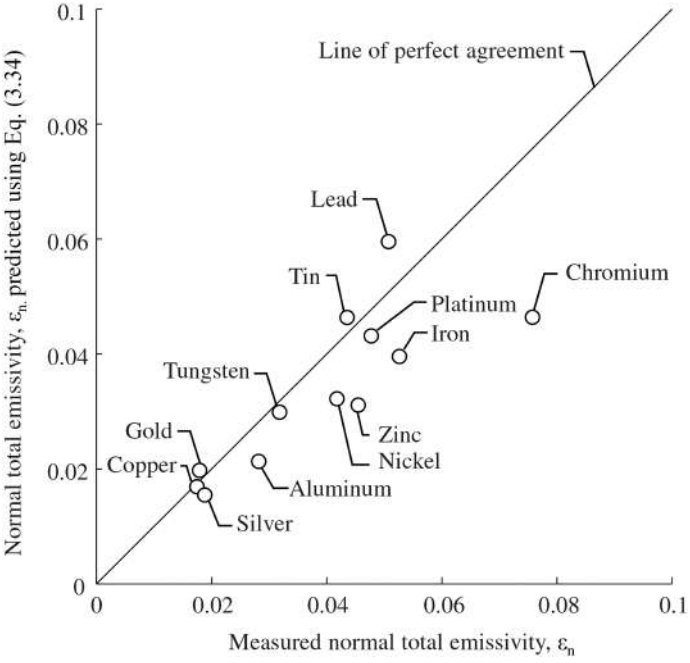

FIGURE 3.10 Comparison of data with calculated normal total emissivity for polished metals at 373 K.

where T and r_e are in units of K and Ω-cm, respectively. The resistivity r_e depends approximately on T to the first power so that the first term of each of these equations provides a T proportionality, indicating that the temperature dependence for energy emission by metals is higher than the blackbody dependence of T^4. A different hemispherical total emissivity expression suggested by Parker and Abbott (1964) is

Figures 3.11 and 3.12 compare predictions for normal total emissivity, Equation (3.32), and hemispherical total emissivity, Equation (3.37), with experimental measurements.

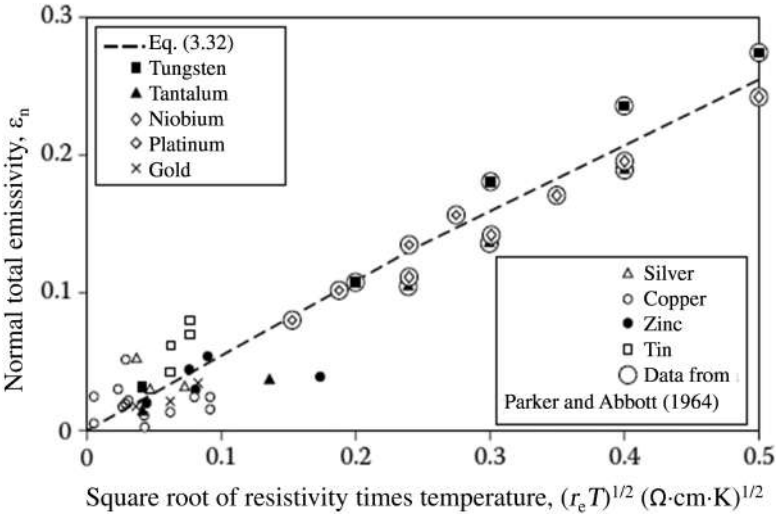

FIGURE 3.11 Normal total emissivity of various metals compared with theory. (From Parker, W.J. and Abbott, G.L., Theoretical and experimental studies of the total emittance of metals, Symposium on Thermal Radiation of Solids, NASA SP-55, pp. 11–28, 1964).

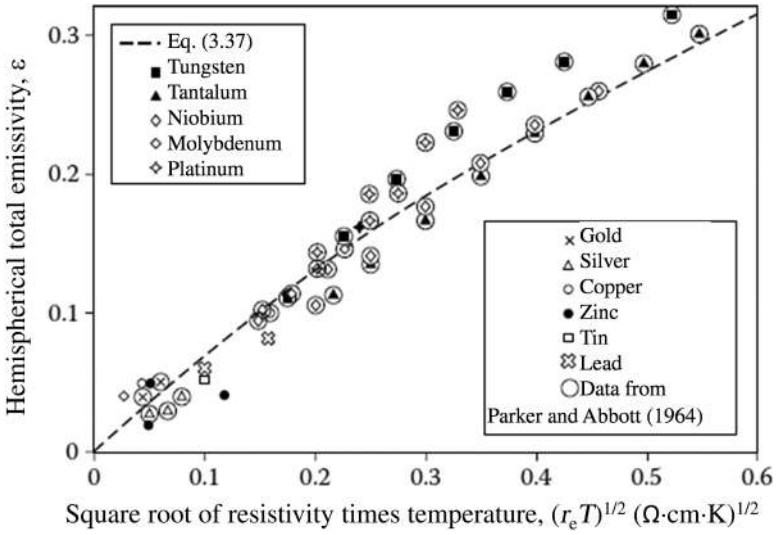

FIGURE 3.12 Hemispherical total emissivity of various metals compared with theory. (From Parker, W.J. and Abbott, G.L., Theoretical and experimental studies of the total emittance of metals, Symposium on Thermal Radiation of Solids, NASA SP-55, pp. 11–28, 1964).

3.2.3 Extensions to the Theory of Radiative Properties

Accurate EM predictions of surface properties requires precise knowledge of the refractive index or dielectric function of the medium. This motivates development of *dispersion* models that account for how these quantities vary with respect to wavelength. A brief discussion concerning dispersion models is presented below; a more complete derivation is included in Chapter 8.

The key difference between metals and dielectrics concerns the nature of the charged particles through which the EM wave interacts with the medium. Charges within dielectrics (e.g., lattice ions or valence electrons) are localized and can be modeled as damped harmonic oscillators that vibrate due to the columbic forces imposed by the local EM field. This model, called the Lorentz model, is highly successful for predicting the variation of the complex dielectric function with respect to the angular frequency of the wave, $\omega = 2\pi\nu = 2\pi c_0/\lambda$

In Equation (3.38), $\omega_{o,j}$ is the resonant frequency, $\omega_{p,j}$ is the plasma frequency, and ζ_j is the damping coefficient for the jth oscillator. These parameters are normally found by nonlinear regression to experimental data. The dielectric function components can then be transformed into n and k via Equation (3.2) if so desired. Figure 3.13 shows the reflectance of MgO predicted using Equation (3.38), which can be modeled using two oscillators (Jasperse et al. 1966). The abrupt variations of spectral reflectivity with respect to wavelength are representative of many dielectrics, and this behavior can be exploited in many engineering applications, e.g., optics and in designing selective surfaces (cf. Section 3.4).

In the case of metals, the EM wave interacts principally (but not exclusively) with conduction band electrons. The classical Hagen–Rubens relations captures this behavior only at long wavelengths, $\lambda >\sim 5$ μm, as outlined by Table 3.2, which shows much better agreement between the predicted and measured $\varepsilon_{\lambda,n}$ value at 10 μm compared to 0.589 μm. This is for two main reasons. First, EM theory presumes that the surface is optically smooth (i.e. the wavelength is much larger than the RMS roughness), which is more likely to be the case at longer wavelengths. Second, Hagen–Rubens theory assumes that electrical conductivity is independent of wavelength; while this is true at long wavelengths, at shorter wavelengths/higher frequencies, electron mobility depends on the

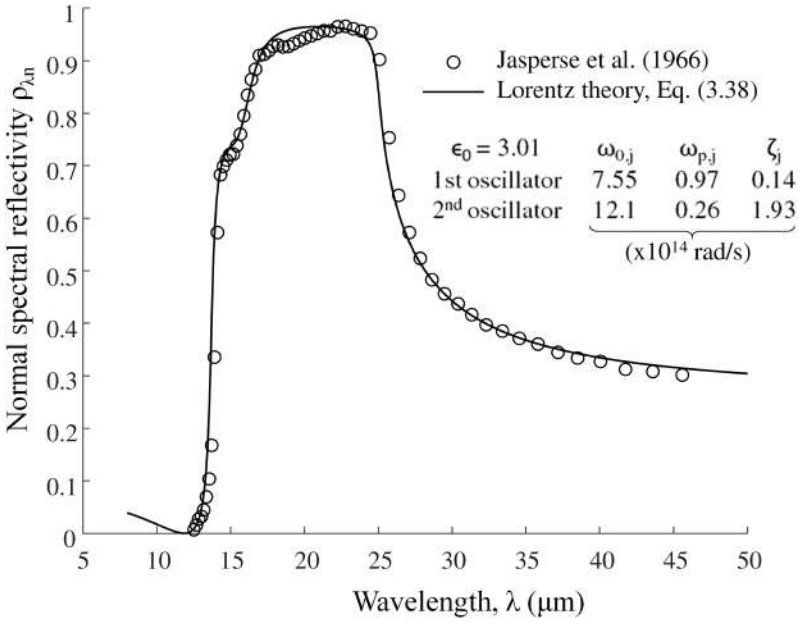

FIGURE 3.13 Normal spectral reflectivity of MgO at room temperature. Lorentz parameters and experimental data from Jasperse, J. R., Kahan, A., Plendl, J. N.: Temperature dependence of infrared dispersion in ionic crystals LiF and MgO, *Phys. Rev.*, 146(2), 526, 1966.

oscillatory motion of electrons induced by the EM wave. This effect is captured by Drude theory, which models the metal as a "sea" of free conduction band electrons that scatter from a background of ions and neutral atoms. The complex dielectric constant is then derived from the damped harmonic motion of electrons:

The Drude parameters in Equation (3.39) are the plasma frequency, ω_p, and the damping coefficient, ζ, which in principle can be calculated from the number density of electrons, N_p, (found from the density and valence of the metal) and DC conductivity, $\sigma_{DC} = 1/r_e$, according to Equations (8.117) and (8.118). Aluminum is particularly well-approximated using Drude theory over the visible and near-infrared wavelengths. Figure 3.14 compares the measured spectral reflectance of polished aluminum and deposited aluminum film with predictions from Hagen–Rubens theory, Equation (3.29), and Drude theory. The Hagen–Rubens prediction is computed using the resistivity for aluminum in Table 3.2, while the Drude parameters of $\omega_p = 2.48 \times 10^{15}$ rad/s and $\zeta = 5.88 \times 10^{12}$ rad/s are also found from r_e and electron number density; the electron number density is found using the bulk density of aluminum, assuming each atom contributes three conduction band electrons.

Drude theory assumes that the EM field interacts exclusively with conduction band electrons; in many metals, however, transitions between bound states (e.g., interband transitions) strongly affect the radiative properties. In some cases Drude theory can still be applied to model the radiative properties of the metal by treating ω_p and τ as parameters to be fitted to reference reflectance data, as opposed to being calculated from the density and DC resistivity of the bulk metal. Ordal et al. (1985) followed this procedure for 14 metals in the infrared and far-infrared. In this scenario Equation (3.39) is simply a convenient means of parameterization; therefore, good agreement between modeled and measured radiative properties should not be construed to mean that Drude theory is an accurate representation of the true electron dynamics within metals in all cases.

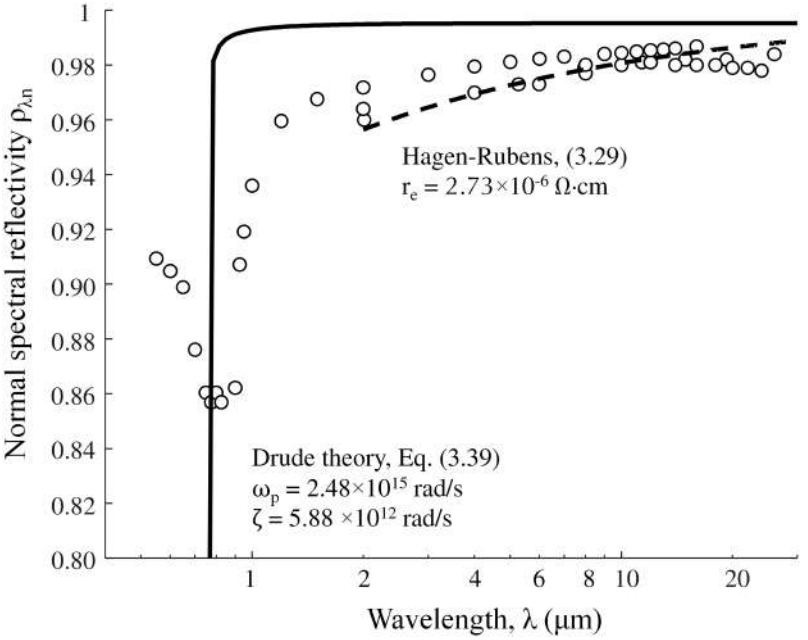

FIGURE 3.14 Normal spectral reflectivity of Ag at room temperature. Drude parameters are calculated using density and DC resistivity. Data from Touloukian, Y.S. and Ho, C.Y. (eds.): Thermophysical Properties of Matter, TRPC Data Services; Volume 7, *Thermal Radiative Properties: Metallic Elements and Alloys*, 1970.

Alternatively, Lorentz–Drude theory can be used to account for transitions between bound states, e.g., the vibration of free electrons.

At still shorter wavelengths (e.g., visible and UV) the role of bound electrons and electron band structure must be considered. The theory for radiative properties of materials has been improved significantly over the years by explicitly modeling these effects. The contributions of Davisson and Weeks (1924), Foote (1915), Schmidt and Eckert (1935), and Parker and Abbot (1964) extended the emissivity relations for metals to shorter wavelengths and higher temperatures, and Mott and Zener (1934) derived predictions for metal emissivity at very short wavelengths on the basis of quantum-mechanical relations. Kunitomo (1984) provides accurate predictions of high- and low-temperature properties of metals and alloys by including the effect of bound electrons on optical properties. Chen and Ge (2000) introduced a damping frequency term into the Drude model of free-electron oscillations, giving a more accurate prediction of the complex dielectric constant. This modifies the relations between the complex refractive index and the complex dielectric constant.

3.3 MEASUREMENTS ON REAL SURFACES

The results discussed in the previous section apply to pure materials having perfectly smooth and uncontaminated interfaces. While there are situations in which these conditions are approximately satisfied, e.g., lenses and optical components, the surfaces encountered in engineering practice more often deviate from this ideal scenario, and their radiative properties will differ significantly from EM predictions.

3.3.1 Heterogeneity and Surface Coatings

In many practical situations the surface may be heterogeneous, which profoundly affects the radiative properties. As an example, in the visible wavelengths, solid ice behaves as a dielectric having a

refractive index of approximately 1.3, so it is nearly transparent at normal incidence (e.g., on sidewalks, much to the chagrin of pedestrians) with a normal reflectance of 0.02 according to Equation (3.14). On the other hand, freshly fallen snow has a reflectivity of approximately 0.85 due to multiple scattering caused by the ice crystals, each of which acts as scattering centers, directing the majority of incident irradiation through multiple scattering events back out of the surface. This phenomenon, sometimes called the "snow effect" (Hollands 2004), is shown schematically in Figure 3.15. Multiple random scattering within the layer dramatically increases the reflectivity and also makes the surface more diffuse-like. The radiative properties of snow are pivotal to climate change, through the overall global radiation budget (i.e. fraction of solar energy reflected vs absorbed) and local changes in climate patterns, which has motivated recent theoretical research and experimental measurements. Ball et al. (2015) measured the bidirectional reflectance function of snow-covered tundra.

The snow effect also applies to paper, fabric, chalk, ceramics, and some pigments and coatings. Figure 3.16 plots the hemispherical normal spectral reflectivity of three paint coatings on steel. White paint often consists of ceramic (e.g., TiO_2) nanoparticles in a silicone or polymer binder and has a high reflectivity at short wavelengths because of the snow effect. Black paint, however, which is often made of absorbing particles like carbon black, has a relatively low reflectivity over the entire wavelength region. Using aluminum powder in a silicone binder produces a reflectivity more representative of a metallic surface.

Coatings based on TiO_2 nanoparticles can be engineered to enhance the solar reflectivity of surfaces (Baneshi et al. 2010), thereby reducing cooling requirements of buildings during summer months. (Spectrally selective surfaces are discussed in Section 3.4 and in Chapter 19). Fuel storage tanks and aircraft are also often treated using white, TiO_2-based paints to prevent them from heating up due to solar radiation. On the other hand, the absorptance of surfaces can be enhanced by embedding highly absorbing particles in a dielectric matrix, e.g., for solar energy applications (Wang et al. 2018). Hadley and Kirchstetter (2012) consider how black carbon particles reduce the high reflectance of snow and ice, along with the implications for climate change. Scattering and absorption of radiation by particles are discussed in more detail in Chapter 10.

Even in the absence of heterogeneities, applying EM theory to dielectrics is complicated by the fact that, for a dielectric to be considered opaque, a specimen must have sufficient thickness to absorb essentially all the radiation that enters through boundaries; otherwise, radiation transmitted through and reflected from all boundaries must be taken into account. Often, then, it is necessary to conceive the dielectric as a coating on a substrate. For a surface to behave completely as the coating material, the coating thickness must be large enough so that no significant radiation is transmitted through it. Otherwise, some incident radiation can be reflected from the substrate and transmitted

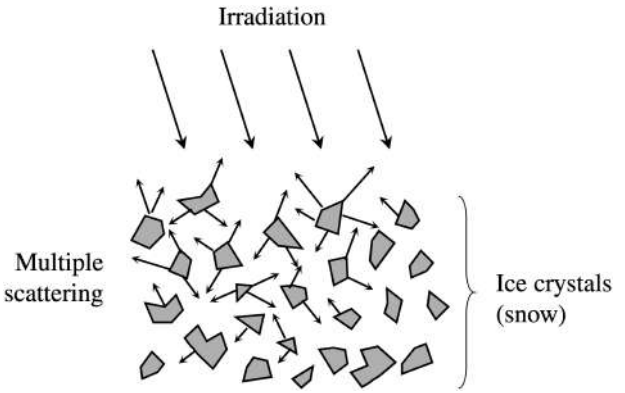

FIGURE 3.15 Heterogeneities in a dielectric can dramatically increase the reflectivity and make the surface more diffuse.

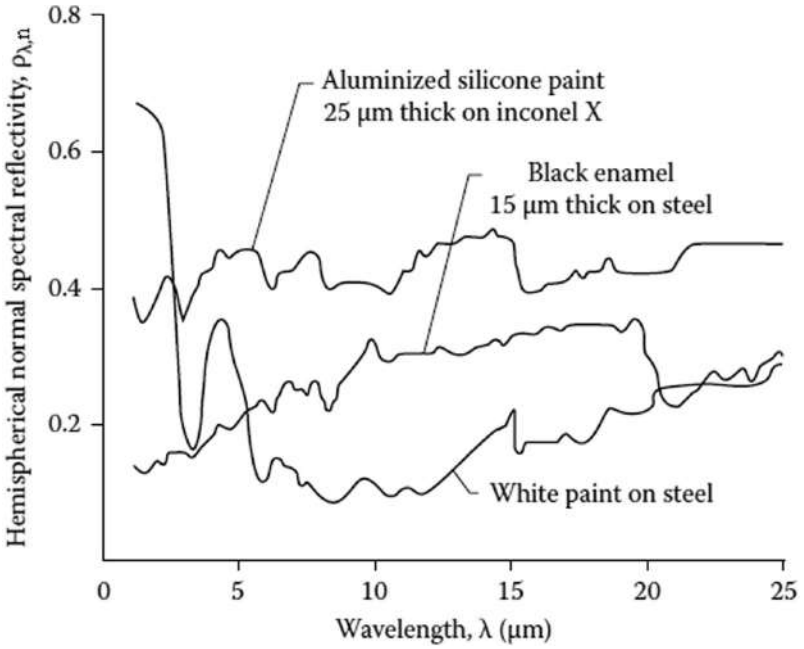

FIGURE 3.16 Spectral reflectance of a TiO_2 based pigment. Data from Touloukian, Y.S. and Ho, C.Y. (eds.), Thermophysical Properties of Matter, TRPC Data Services; Volume 9 *Thermal Radiative Properties: Coatings, 1972b.*

back through the coating to reappear as measured reflected energy, in which case the surface properties would depend on both the coating material and thickness and the substrate.

One of the earlier studies on this subject was conducted by Liebert (1965), who examined the spectral emissivity of zinc oxide coatings on various substrates. In Figure 3.17, the effect of coating thickness is shown on the spectral emissivity of a composite of zinc oxide on a substrate that has an approximately constant normal spectral emissivity. The effect of increasing coating thickness becomes small in the thickness range of 0.2–0.4 mm, indicating that the emissivity approaches that of zinc oxide alone. Figure 3.18 shows the spectral reflectance of a 14.4 μm TiO_2 paint film on various substrates. It is clear that the substrate may have a considerable impact on the spectral reflectivity. For a black substrate, as the wavelength decreases and becomes small relative to the film thickness, the reflectivity increases and becomes more like that of the white paint film.

The most common surface impurities on metal surfaces are thin layers deposited either by absorption, such as water vapor, or by chemical reaction, such as a thin oxide layer. Because dielectrics generally have high emissivities, an oxide layer or other nonmetallic contaminant usually increases the emissivity of an otherwise ideal metallic surface. Figure 3.19 shows the directional-spectral emissivity of titanium at $\theta = 25°$ (Edwards and Catton 1964, Edwards and Bayard de Volo 1965). The data points are for unoxidized metal, and the solid line is the ideal emissivity predicted by EM theory. The dashed curve is the observed emissivity when the surface is contaminated with a 0.06 μm thick oxide layer, which nearly doubles ε_λ compared to pure titanium over much of the wavelength range. Similarly, Figure 3.20 shows how oxidation affects the normal spectral emissivity of Inconel X over visible and near-infrared wavelengths (Wood 1964). Finally, Figure 3.21 shows how the normal total emissivity of copper and the hemispherical total emissivity of aluminum change with oxide layer thickness. The copper oxide layer was produced by heating copper in air, while the aluminum oxide layer was produced through anodization. The emissivity of both metals is initially very low (typical for a highly conducting metal) but increases as the oxide coating becomes thicker. The surface roughness of the oxide layer may also evolve as it grows, as discussed in Section 3.3.2.

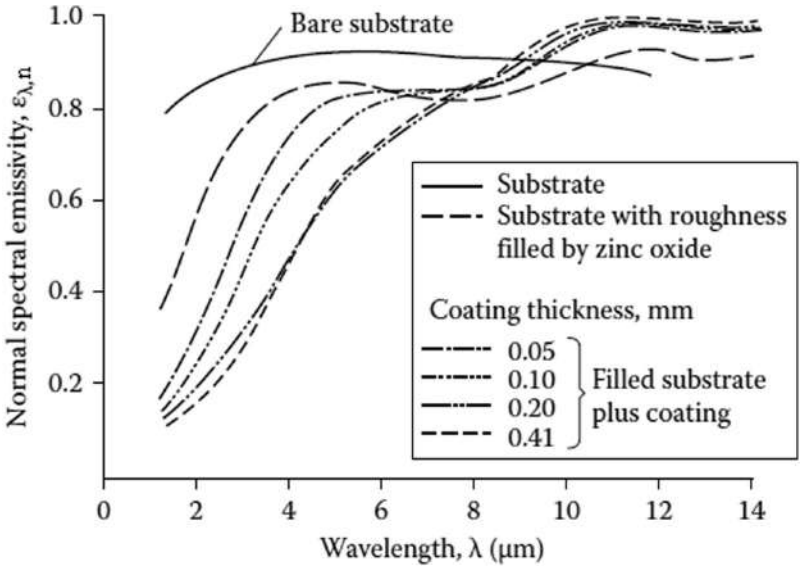

FIGURE 3.17 Spectral emissivity of zinc oxide coatings on an oxidized stainless-steel substrate. (From Liebert, C. H., Spectral emittance of aluminum oxide and zinc oxide on opaque substrates, NASA TN D-3115, 1965).

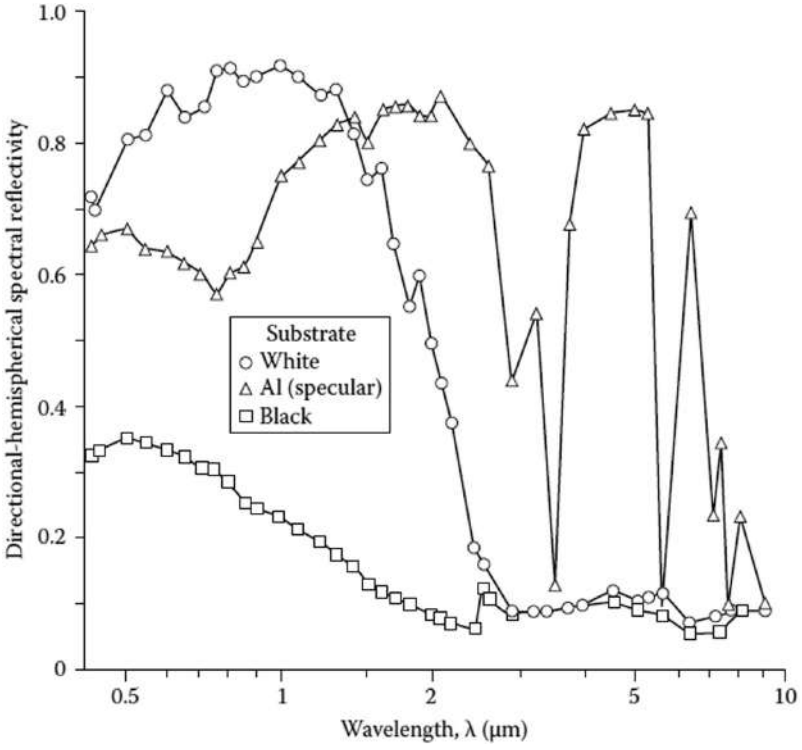

FIGURE 3.18 Effect of substrate reflectivity characteristics on the hemispherical-spectral reflectivity of a TiO_2 paint film for normal incidence. Film thickness, 14.4 μm; volume concentration of pigment, 0.017. (From Shafey, H.M. et al., *AIAA J.*, 20(12), 1747, 1982).

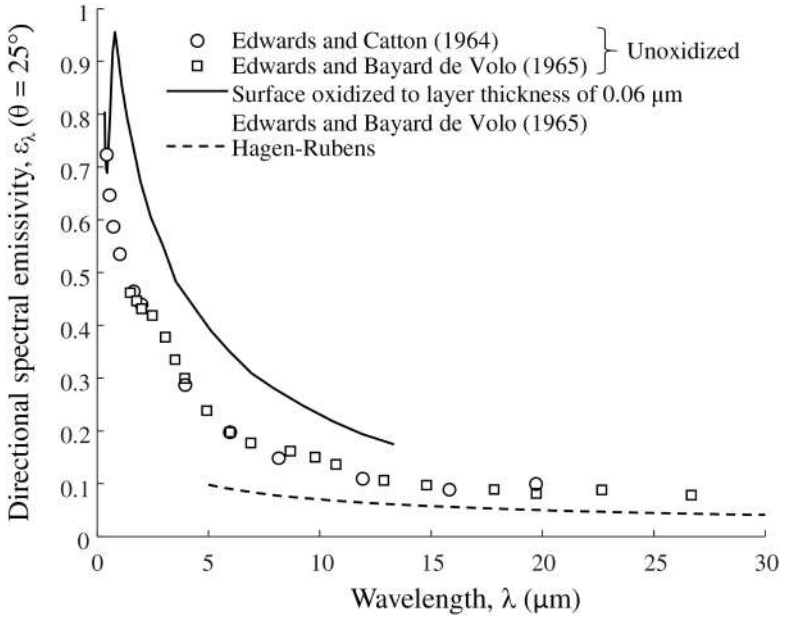

FIGURE 3.19 Effect of oxide layer on directional-spectral emissivity of titanium. Emission angle, $\theta = 25°$; surface lapped to 0.05 mm RMS; temperature 294 K.

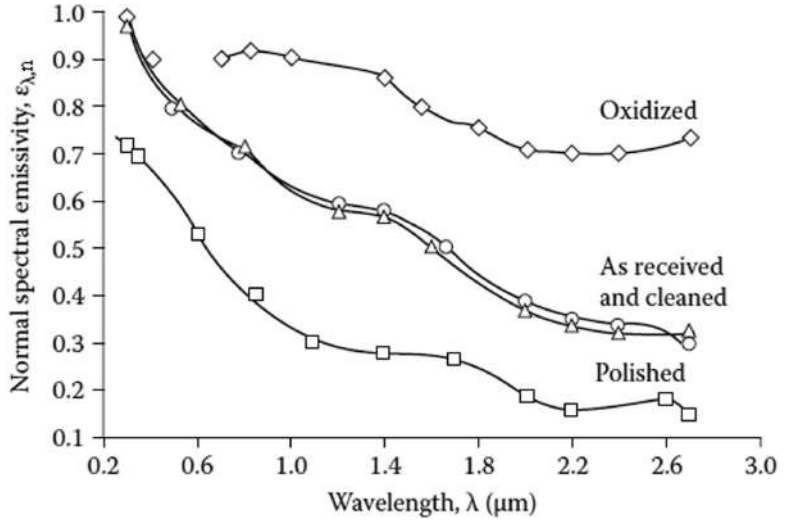

FIGURE 3.20 Effect of oxidation on normal spectral emissivity of Inconel X. (Data from Wood, W. D., et al., *Thermal Radiative Properties*, Plenum Press, New York, 1964).

In some cases, an oxide film can induce oscillatory patterns in ε_λ or ρ_λ due to the phase shift caused by the oxide layer, leading to constructive and destructive interferences between the incident and reflected EM wave. Figure 3.22 shows the spectral emissivity of an iron surface heated in air as a function of time (del Campo et al. 2008.) The rate at which the peaks shift is connected to the oxide layer growth, which is used to infer the oxidation reaction kinetics. Makino et al. (1988) reported similar results for oxide layers on chromium. This effect is also responsible for the attractive colors of anodized metals, which can be controlled through careful engineering of the oxide layer thickness. Thin film interference effects are discussed further in Chapter 17.

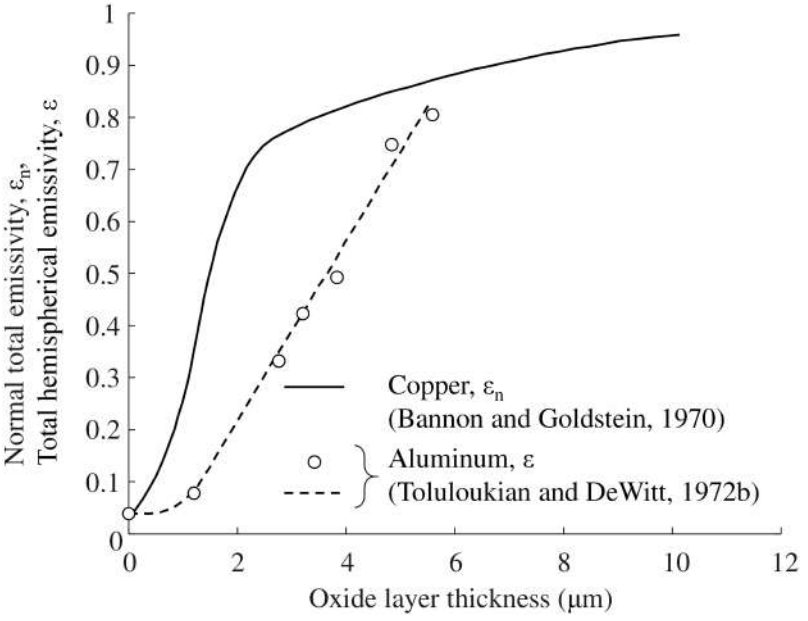

FIGURE 3.21 Effect of oxide layer thickness on the normal total emissivity of copper and hemispherical total emissivity of aluminum. Data for copper: Brannon, R. R., and Goldstein, R. J., *ASME J. Heat Trans.*, 92(2) 257, 1970. Data for aluminum: Touloukian, Y.S. and Ho, C.Y. (eds.), Thermophysical Properties of Matter, TRPC Data Services, Volume 9, *Thermal Radiative Properties: Coatings*, Touloukian, Y.S., DeWitt, D.P., and Hernicz, R.S. (1972b).

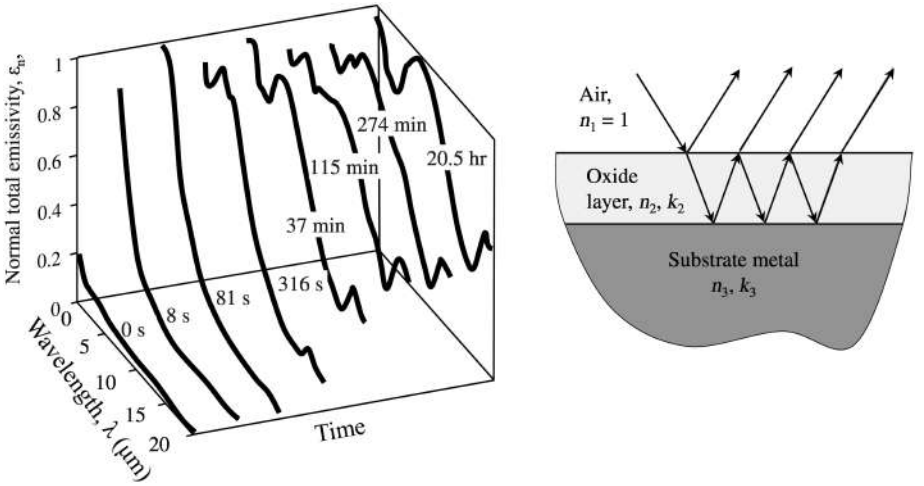

FIGURE 3.22 Thin film interference effect due to oxide layer growth. From del Campo, L. Pérez-Sáez, R. B., Tello, M. J.: Iron oxidation kinetics study by using infrared spectral emissivity measurements below 570°C, *Corros. Sci*. 50, 194, 2008.

3.3.2 Surface Roughness Effects

Surface topography has a profound and varied impact on the radiative properties of metals and nonmetals, depending on the bulk refractive index of the surface and the size of the surface features relative to wavelength. While surfaces may appear smooth macroscopically, microscopically they consist of asperities that may be induced by the manufacturing process, mechanical damage, or

a chemical reaction (e.g., oxidation). In some cases, microscale roughness may be imparted with the specific intent of altering the radiative properties of a surface. If the process that caused the roughness is random, it is often reasonable to approximate the roughness as a sequence of normally distributed peaks, where the asperity heights z follow a normal distribution

where σ_o is the root-mean-square (rms) roughness, (sometimes written R_q)

the mean surface height is z_m, and $\langle\cdot\rangle$ represents the average, as shown in Figure 3.23. The rms roughness is readily measured using a contact profilometer, consisting of a stylus or needle that is dragged across a surface. The rms roughness is then used to derive the "optical roughness," σ_o/λ. At small values of optical roughness, the surface may appear specular or "mirror-like," while at large values the reflection may be more diffuse in nature. For this reason, many surfaces that appear diffuse at visible wavelengths can often be approximated as specular in the infrared. A good demonstration of this phenomenon involves looking at a classroom whiteboard with an infrared camera; the board reflects visible light diffusely, while a clearly defined image of the reflected body heat from the camera operator is visible in the infrared because the white board is optically smooth at these wavelengths.

Generally, when σ_o/λ is greater than about unity, multiple reflections occur in the cavities between roughness elements; this increases the trapping of incident radiation, thereby increasing the observed surface absorptivity and consequently the emissivity. Graphite has one of the highest emissivities of commonplace materials due in part to its porous structure, and consequently it is often used to construct surfaces having radiative properties that mimic those of a blackbody.

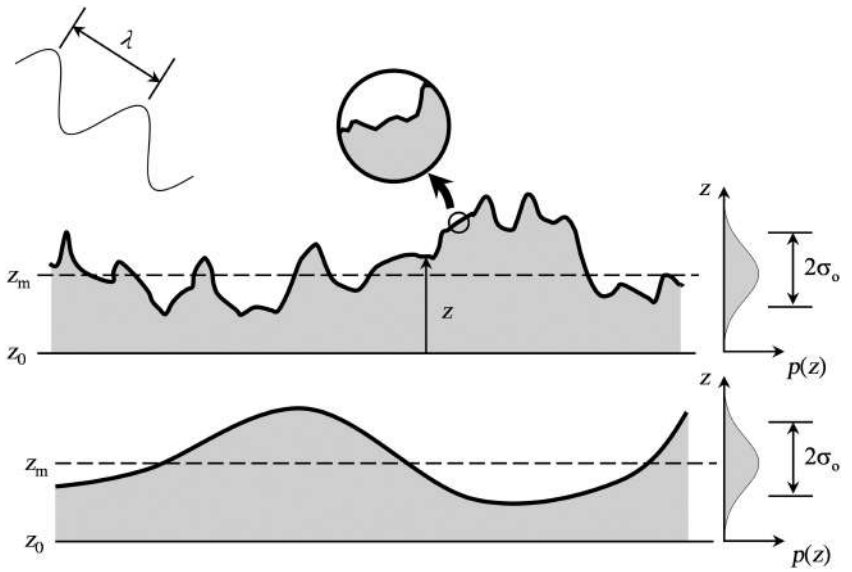

FIGURE 3.23 Definition of RMS roughness. Both surfaces shown here have similar RMS roughness, but would have different radiative properties. Moreover, roughness exists at different scales, which interact with an EM wave in different ways depending on the wavelength.

VantaBlack™ enhances this effect via a field of closely packed and vertically aligned carbon nanotubes, giving it an even higher emissivity than that of graphite (Theocharous et al. 2006).

Surface roughness may be caused by the manufacturing process, or it may be due to chemical reactions like oxidation. Figure 3.24 shows the normal spectral emissivity of three types of aluminum surface: commercial aluminum, mechanically polished aluminum and a surface formed by ultrahigh vacuum deposition of aluminum onto a quartz surface. The spectral emissivity is largest for the roughest sample and is smallest for the smoothest surfaces. The influence of roughness is most pronounced at the short wavelengths, where the optical roughness is the largest.

Williams et al. (1963) showed that the hemispherical-spectral emissivity of an aluminum surface coated with lead sulfide is a strong function of the crystalline structure of the lead sulfide, which may appear as cubes or dendrites. In a more recent study, Yu et al. (2019) attribute variations in spectral emissivity of copper surfaces oxidized in air at various temperatures and durations to the differing surface morphology of the oxides, as shown in Figure 3.25.

Shi et al. (2015) measured the spectral emissivity of steel sheets coated with an Al-Si layer, which prevents oxidation and decarburization of the steel during furnace heating. The hemispherical-spectral emissivity is plotted in Figure 3.26 at various stages of furnace heating. The radiative properties of the as-received aluminum coating are typical of a metallic surface having a roughness in the order of 1–2 μm and is similar to the normal spectral emissivity of commercial aluminum in Figure 3.24. The coating melts at approximately 575°C, giving the surface a very low emissivity, characteristic of a smooth, highly conducting metal. At higher temperatures the coating reacts with iron from the substrate steel to form an intermetallic layer having radiative properties more representative of an insulator. The emissivity continues to increase with heating due to the increasing surface roughness. This effect is highlighted by examining the evolving spectral emissivity of samples heated in air and argon. The argon-heated samples are much smoother, and consequently have a lower spectral emissivity compared to the ones heated in air, as shown in Figure 3.27.

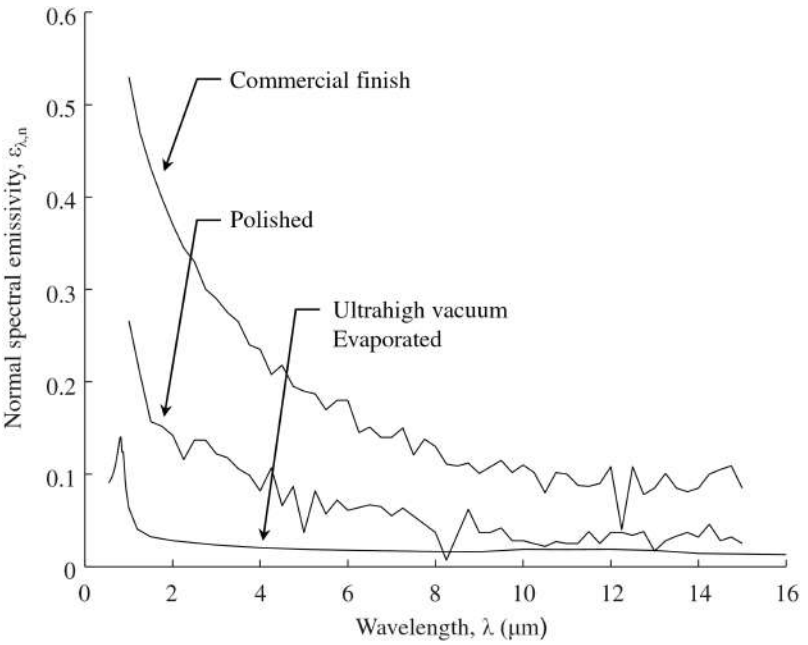

FIGURE 3.24 Normal spectral emissivity of aluminum surfaces having different surface finishes. Data from Touloukian, Y.S. and Ho, C.Y. (eds.), Thermophysical Properties of Matter, TRPC Data Services; Volume 7, *Thermal Radiative Properties: Metallic Elements and Alloys*, 1970.

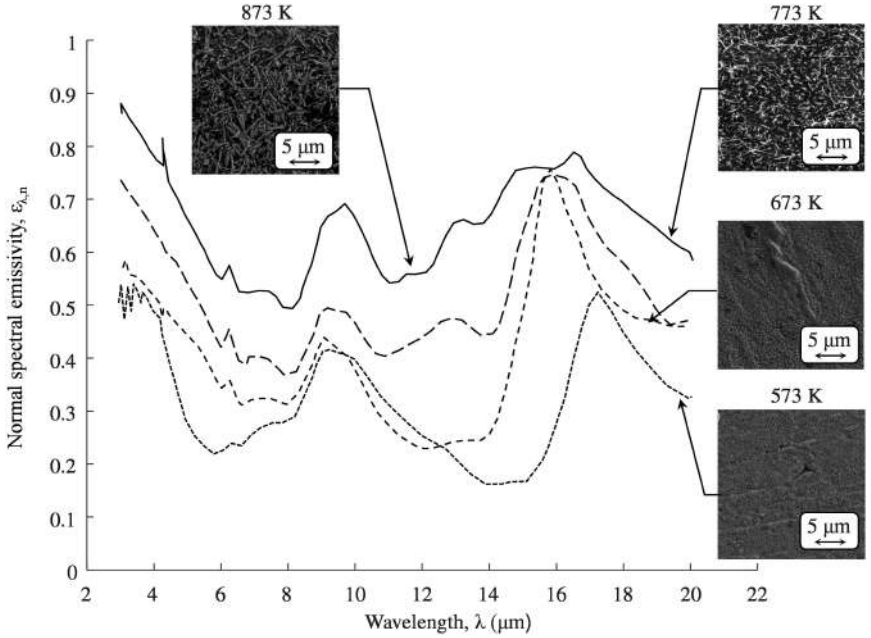

FIGURE 3.25 Normal spectral emissivity of copper surfaces heated in air for 1 hr at different soak temperatures. Scanning electron micrographs show the corresponding surface topographies. From Yu, K., Zhang, H., Liu, Y., Liu, Y.: Study of normal spectral emissivity of copper during thermal oxidation at different temperatures and heating times, *IJHMT*, 129, 1066, 2019.

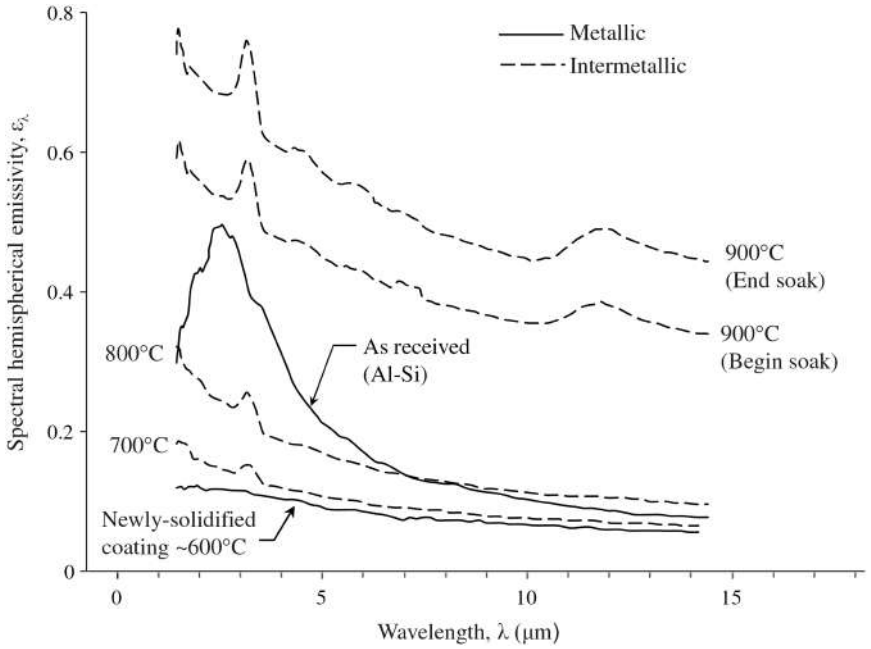

FIGURE 3.26 Spectral emissivity of Al-Si coated 22MnB5 steel. (Data from ArcelorMittal).

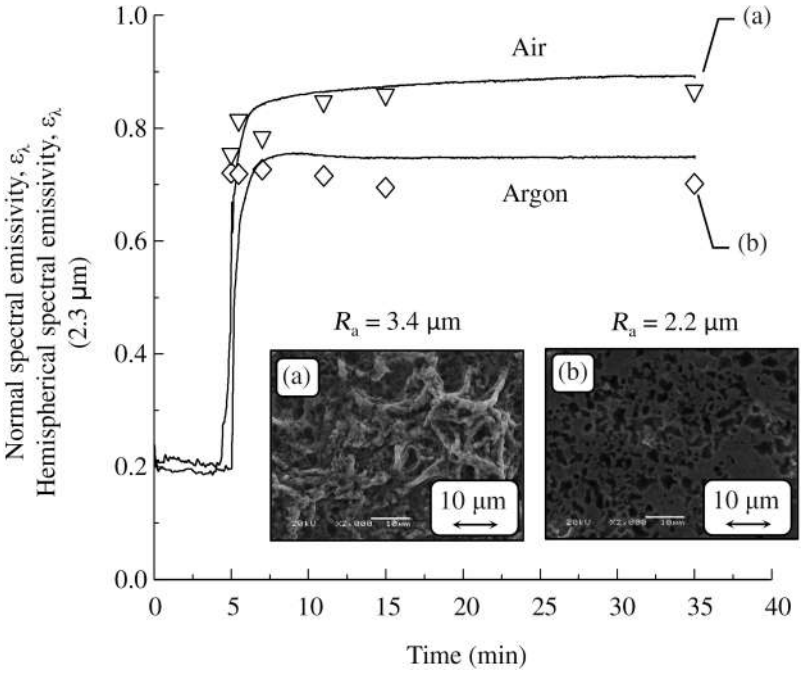

FIGURE 3.27 Influence of atmosphere on surface morphology and spectral emissivity of Al-Si coated 22MnB5 steel during two-step heating. The samples are initially heated at 610°C for 5 minutes and then 900°C for varying durations. Solid curves show in-situ normal spectral emissivity measurements, while symbols show ex-situ hemispherical spectral emissivity. Arithmetic roughness (R_a) was measured with a contact profilometer. From Shi, C. J., Daun, K. J., and Wells, M. A.: Spectral emissivity characteristics of the Usibor® 1500P steel during austenitization in argon and air atmospheres, *IJHMT,* 91, 818, 2015.

While spectral emissivity generally increases with surface roughness, this is not always the case. Cox (1965) showed that for dielectric materials with $\sigma_o\beta_\lambda$, a ratio of roughness to mean penetration distance in the material of about 0.05 (the mean penetration distance is $l = 1/\beta_\lambda$), the emissivity may be less than a smooth surface. This can be considered as an extension of the "snow effect" described in the preceding section.

Surface roughness also affects the directional nature of emission and reflection. Figure 3.28 shows the ratio of the reflectivity in the specular direction of a rough nickel surface compared to that of a polished specimen, which increases as σ_o/λ becomes large. Figure 3.29 shows the bidirectional spectral reflectivity of an aluminum surface having an optical roughness of σ_0/λ of 2.6 in the incidence plane (*cf.* Figure 3.1.) Detailed bidirectional reflectivity measurements for magnesium oxide ceramic with optical roughness σ_o/λ varying from 0.46 to 11.6 are listed by Torrance and Sparrow (1966). As the roughness and incidence angle of the incoming radiation are increased, off-specular peaks are obtained. Bidirectional-spectral reflectivity measurements are reported by DeSilva and Jones (1987) for six materials used for solar energy absorption. Peaks in the specular direction were found.

Drolen (1992) provides bidirectional reflectivity measurements for 12 materials commonly used for spacecraft thermal control, such as white paint, black Kapton, and aluminized Kapton. The "specularity" given is the fraction of the directional-hemispherical reflectivity contained within the specular solid angle. Specularity values can be used in surface property models that assume a combination of diffuse and specular reflectivities (*cf.* Sections 6.5 and 6.6). Most measurements reported by Drolen are at a wavelength of $\lambda = 0.488$ μm, but some white paints were measured at four discrete wavelengths covering the range $0.488 \le \lambda \le 10.63$ μm. Zaworski et al. (1996a) present detailed bidirectional reflectance data for a variety of surfaces, including Krylon white paint.

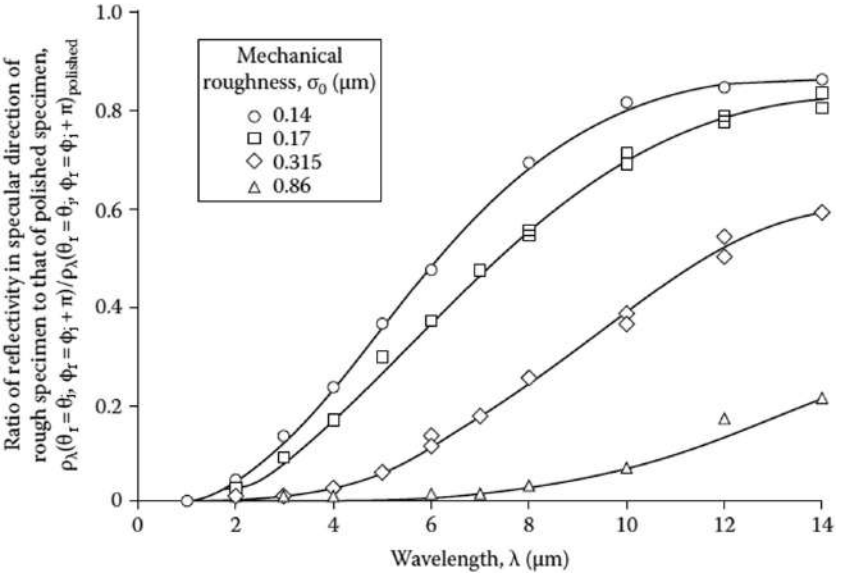

FIGURE 3.28 Effect of roughness on bidirectional reflectivity in the specular direction for ground nickel specimens. Mechanical roughness for polished specimen, 0.0015 μm. (From Birkebak, R. C., and Eckert, E. R. G., *JHT*; 87(1) 1965).

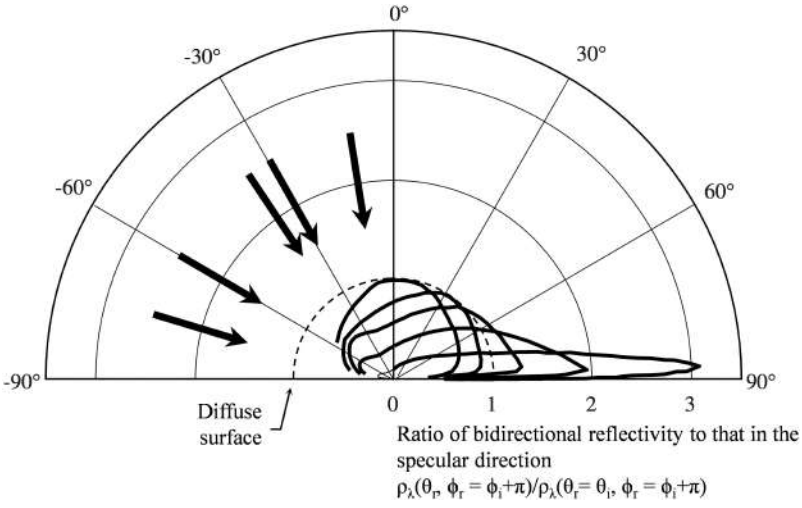

FIGURE 3.29 Bidirectional reflectivity in the incidence plane for various incidence angles; 2024–T4 aluminum (coated); $\sigma_o = 1.3$ μm; wavelengths of incident radiation, $\lambda = 0.5$ μm. (From Torrance, K. E., and Sparrow, E. M., *JOSA*, 57(9), 1105, 1967).

Figure 3.30 shows that the painted surface is quite diffuse until incident angles of 60° or greater are reached. Combined, the results suggest that the bidirectional reflectivity can be modeled as the superposition of a diffuse reflector and a specular reflector. This approximation has merit in some cases and simplifies the radiant exchange calculations compared with using exact directional properties (Sparrow and Liu 1965, Sarofim and Hottel 1966).

In other cases, however, this approximation would fail. A particularly interesting example concerns the lunar surface, which is highly reflective due to its roughness and porosity. When the moon is full in phase, the sun, earth, and moon are nearly coincident and the moon is uniformly

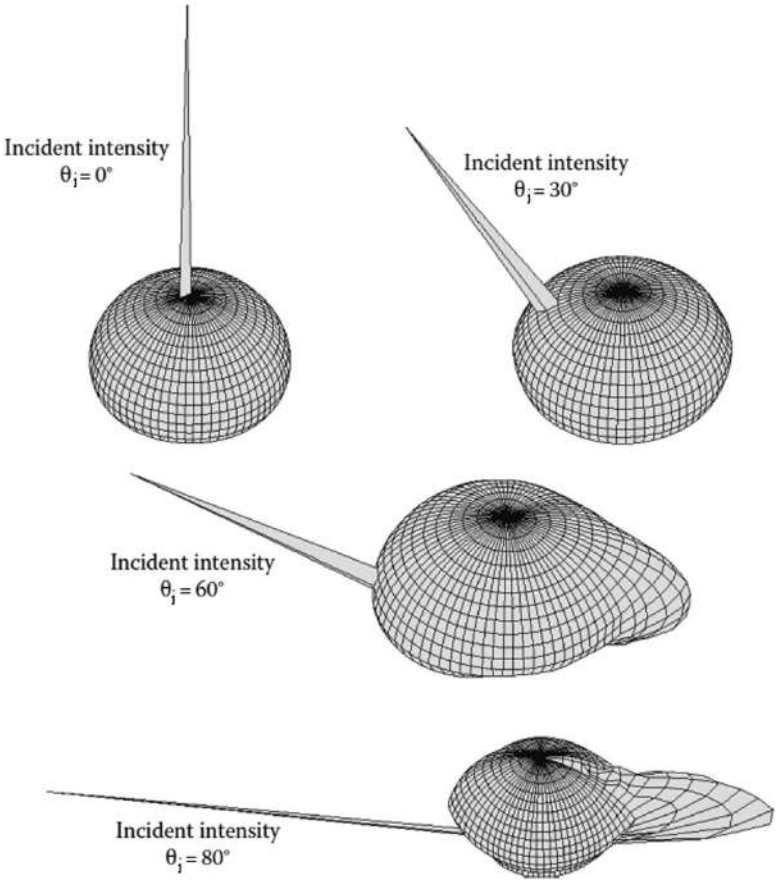

FIGURE 3.30 Bidirectional reflectivity of Krylon white paint. Plots are of $\ln[\rho_\lambda(\lambda,\theta_i,\phi_i, \theta_r, \phi_r)]$ at $\lambda = 0.6328$ μm. (From Zaworski, J. R., et al., *IJHMT*, 39(6) 1149, 1996a).

irradiated with nearly collimated solar radiation, as shown in Figure 3.31. Were the lunar surface diffuse, as one may expect for a rough surface, the reflected light would follow a Lambertian cosine distribution, and the moon would appear brightest at its center and darker near its edges. On the contrary, however, we see the moon as a white disk of nearly uniform intensity. The reason for this observation can be traced back to the bidirectional reflectivity measurements plotted in Figure 3.32 that show a strong back-scattering component, located 180° away from the direction of specular reflectance (Orlova 1956). Consequently, the bidirectional reflectance component increases approximately proportional to $1/\cos\theta_i$ (shown by the dashed line in Figure 3.32). This compensates for the reduced energy incident per unit area at large angles. Further discussions of the radiative properties of the lunar surface are given by Saari and Shorthill (1967), Harrison (1969), Birkebak (1974), and Sailsbury et al. (1997). Ohtake et al. (2013) describe recent measurements carried out from a lunar orbiter.

While optical roughness provides a general indication of the importance of surface topography over a particular spectrum and can be used to interpret trends in the data, it is inadequate to make quantitative predictions of radiative properties. It does not account for the horizontal spacing of the roughness, for example, nor does it indicate the *distribution* of the roughness size around the rms value (which may not be normally distributed), nor information on the average slope of the sides of the roughness peaks. Both surfaces shown in Figure 3.23 may have the same rms roughness, but the slopes and spacing between the asperities are quite different, which would lead to dissimilar

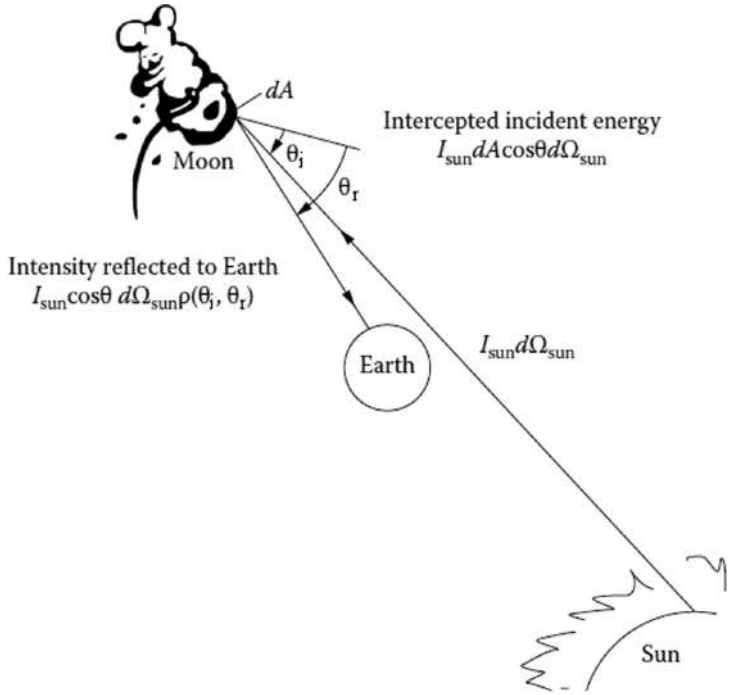

FIGURE 3.31 Reflected energy at full moon. (Not to scale).

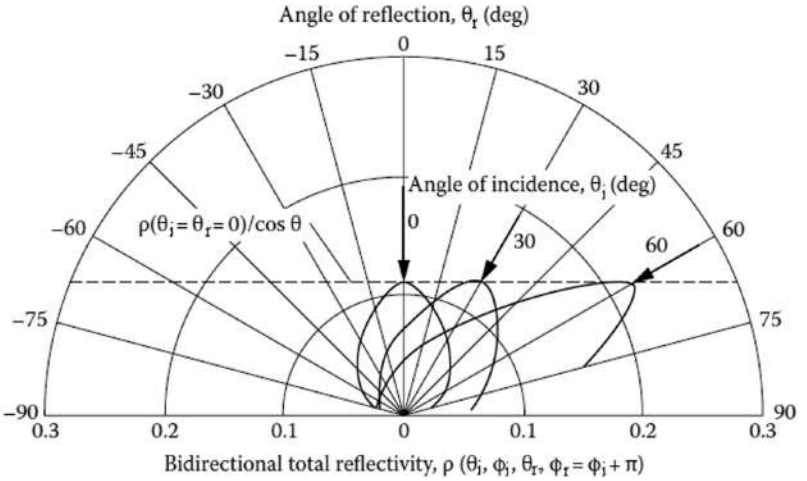

FIGURE 3.32 Bidirectional total reflectivity in the incidence plane for mountainous regions of the lunar surface. After Orlova, N. S. *Astron. Z.* 33(1), 93, 1956).

radiation properties. A further complication is that surface topography exists at multiple scales, and often has a self-similar, "fractal like" quality (Majumdar and Tien 1990a, 1990b) that is not captured by the rms roughness measured by contact profilometry. The influence of additional geometric scales that characterize surface roughness is also addressed by Yang and Buckius (1995). An important example concerns the radiative properties of metals, which are needed to carry out multiwavelength pyrometry during thermal processing. The spectral emissivity of these alloys is known to evolve due to oxide nodules that appear as the steel is heated within a reducing atmosphere. However, contact profilometry measurements made on samples extracted from a furnace at

intermediate heating times did not correlate with the changing emissivity; this is because the rms roughness measured using the contact profilometer was dominated by large-scale rolling artifacts that did not influence the radiative properties of the specimen (Ham et al. 2018).

Additional parameters and more sophisticated measurement techniques are therefore needed to derive quantitative estimates of radiative properties. Some contact profilometers provide the average surface slope, or additional "skewness" and "kurtosis" parameters to describe the shape of the asperities. The local radius of curvature and spacing between asperities are also important. For randomly rough surfaces this latter quantity can be quantified by the Gaussian correlation function

where τ is the correlation length, which is the width of a Gaussian correlation function over which the roughness correlation decreases by a factor of e.

Optical profilometers use the principle of interferometry to construct a "2D" picture of roughness. Many of these instruments provide a "power spectrum" of the surface topography, showing the prominence of different length scales in accordance with the fractal-like nature of surface roughness. Still higher resolution can be obtained through atomic force microscopy (AFM), which have horizontal and vertical resolution on the order of ~30 nm and 0.1 nm, respectively. Example optical and AFM profilograms are shown in Figure 3.33.

Detailed surface topography information can sometimes be used to derive theoretical or numerical models for radiative properties of surfaces. Wen and Mudawar (2006) present a taxonomy of models used to predict the spectral emissivity of metallic surfaces, shown in Figure 3.34. These surfaces can broadly be categorized as perfectly smooth; slightly rough; moderately rough; and very rough. A schematic of the bidirectional reflectances that correspond to this case is shown in Figure 3.35.

The radiative properties of perfectly smooth surfaces can be modeled directly using the relations in Section 3.2.2. For slightly rougher surfaces, small surface asperities act as "scattering centers" for the incident wave, and the observed radiative properties are due to the superposition of the scattered waves in the far field. Davies (1954) derived an analytical model using the Kirchhoff approximation,

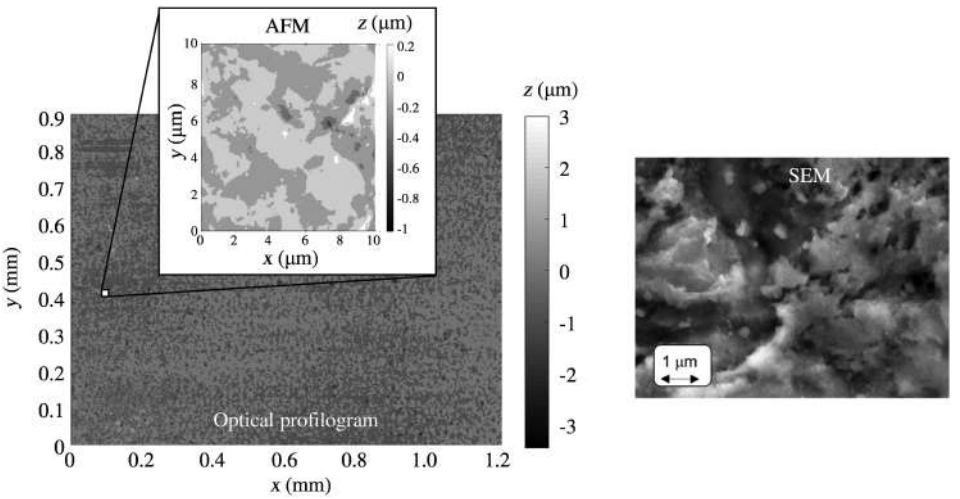

FIGURE 3.33 Optical profilogram, atomic force micrograph, and scanning electron micrograph of DP980 steel alloy heated in a reducing atmosphere. (The box outline on the optical profilogram does not coincide with the AFM region, but emphasizes scale.) Liu, K., and Daun, K. J.: Interpreting the spectral reflectance of advanced high strength steels using the Davies' model, *JQSRT*, 242, 106796, 2020.

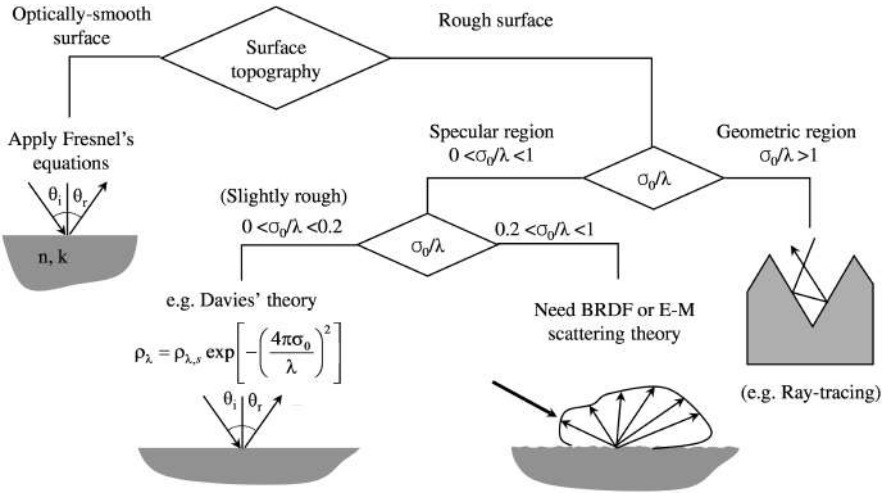

FIGURE 3.34 Types of models used to predict spectral emissivity of metallic surfaces. Wen, C.-D and Mudawar, I.: Modeling the effects of surface roughness on the emissivity of aluminum alloys, *IJHMT*, 49, 4279, 2006.

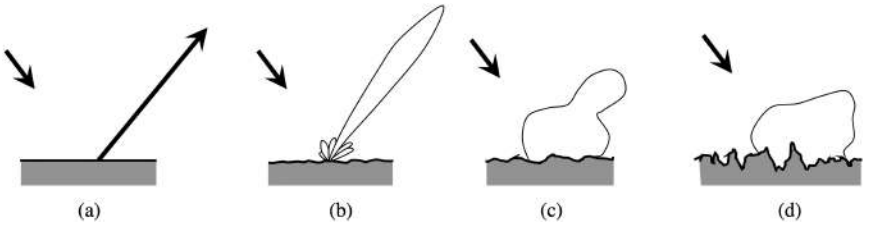

FIGURE 3.35 Transition from specular reflectance to diffuse scattering. Surfaces are: (a) smooth; (b) slightly rough; (c) moderately rough; (d) very rough. Beckman, P., and Spizzichino, A.: *The Scattering of Electromagnetic Waves from Rough Surfaces*, Pergamon Press, New York, 1963.

in which the Fresnel reflection equations are applied to the tangent plane of the surface roughness at each point of incidence; this may be reasonable, provided that the local radius of curvature is less than the wavelength, and the correlation length is sufficiently large. The material is further to be a perfect electrical conductor so that, from EM theory, the extinction coefficient is infinite. This provides perfect reflection, and consequently, the theory gives the directional distribution of the energy that is reflected distribution about the specular peak as shown in Figure 3.35b, as opposed to the reflectivity. According to this theory the reflectance in the specular direction is given by

which diminishes as the surface becomes optically rough and the lobular scattering pattern in Figure 3.35b becomes broader. This treatment can be extended to surfaces having finite conductivity by introducing a coefficient $\rho_{\lambda,s}$ to the right-hand side of Equation (3.43) that equals the reflectance of a perfectly smooth surface made of the same material (e.g., from Fresnel's relations). Davies treatment is inaccurate at near-grazing angles because shadowing by the roughness element *s* is neglected.

Modeling the radiative properties of a moderately rough surface is considerably more complex. Porteus (1963) extended Davies approach by removing the restrictions on the relation between σ_0

and λ and including more parameters for specifying the surface roughness characteristics. Some success was obtained in predicting the roughness characteristics of prepared samples from measured reflectivity data. Measurements were mainly at normal incidence, and the neglect of shadowing makes the results doubtful at near-grazing angles.

Beckmann and Spizzichino (1963) also extend the applicability of Davies' theory by accounting for the autocorrelation distance of the roughness, τ. The method provides better data correlation than the earlier analyses and captures the more diffuse reflectance that one would expect for large values of optical roughness. A critical evaluation of Davies and Beckmann analyses is given by Houchens and Hering (1967). Data for aluminum have been well-correlated in Smith and Hering (1970) by use of Beckmann's theory.

The emissivity of a surface with random submicron roughness elements is discussed by Carminati et al. (1998) and Ghmari et al. (2004). Through scaling arguments, it is shown that interference effects between radiation emitted by closely spaced elements can be neglected, which is not the case for reflected energy. Based on this observation, predictions of directional-spectral emissivity from surfaces with random submicron roughness elements can be made through numerical simulation. Because the model initially neglects shadowing and blocking effects, the predictions are restricted to rms height to wavelength ratios of $\sigma_o/\lambda < 0.3$, as obtained by comparison with experimental emissivity data for the two components of polarization.

Figure 3.36 shows the spectral hemispherical reflectivity of a steel alloy measured with an integrating sphere, along with the near-normal specular reflectance and diffuse reflectance, which excludes the specular component from the hemispherical reflectivity. The surface topography is dominated by large-scale rolling artifacts (seen in the optical profilogram of Figure 3.32) and oxide nodules having diameters of around 100 nm at smaller scales, seen in the atomic force and scanning electron micrographs. The profilometer-derived rms roughness is 0.42 μm. At long wavelengths ($\lambda > 15$ μm) the surface is "slightly rough" and the specular reflectance approaches the hemispherical reflectance, indicating that the surface behaves in a specular manner and ρ_λ can be modeled

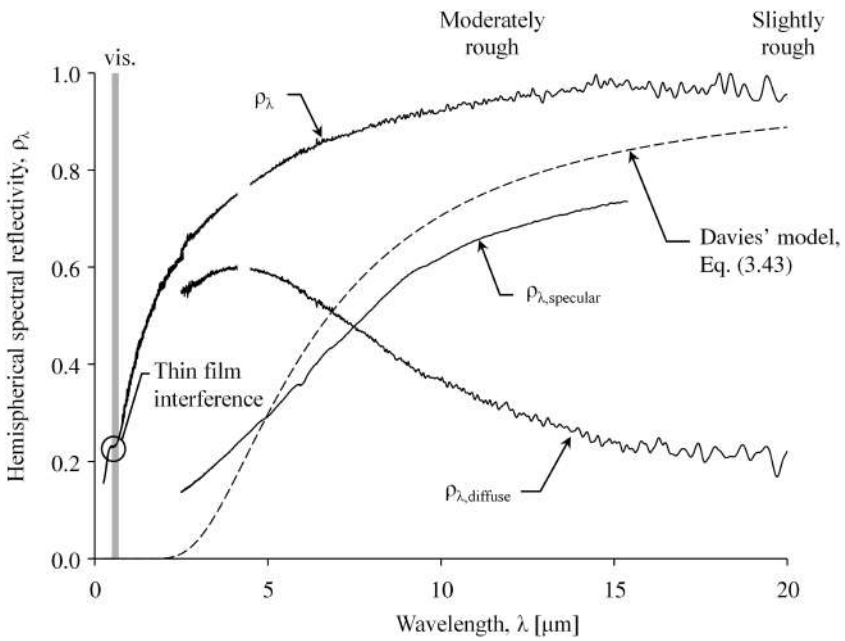

FIGURE 3.36 Spectral hemispherical reflectance of DP980 steel alloy annealed in a reducing atmosphere. Liu, K., and Daun, K. J.: Interpreting the spectral reflectance of advanced high strength steels using the Davies' model, *JQSRT*, 242, 106796, 2020.

using Equation (3.43). At shorter wavelengths the surface becomes moderately rough, as indicated by the drop in the specular reflectivity and an increase in the diffuse reflectivity. At still shorter wavelengths ($\lambda < 1$ μm) a ~100 nm thick passivating oxide film causes an oscillation in ρ_λ according to the wave-interference theory presented in Section 3.3.2. This behavior alters the visible appearance of the steel surface.

For $\sigma_o/\lambda \gg 1$, geometric optics may be used to trace the radiation paths reflected within cavities formed by the roughness elements, and if the roughness geometry is completely specified, it is possible in certain cases to predict the directional behavior. Ordinarily, roughness is very irregular, and a statistical model must be assumed. For example, roughness can be represented as randomly oriented facets that each reflect in a specular manner. A roughness model composed of spherical cap indentations was also suggested by Demont et al. (1982). Ody Sacadura (1972) and Kanayama (1972) analyzed the angular distribution of the emissivity from a rough surface by considering emission from V-grooves in a parallel or circular pattern. A more realistic model is the randomly roughened metal surface in Abdulkadir and Birkebak (1978) and Wolff and Kurlander (1990) where multiple reflections between surface elements were neglected. Calculations for gold and chromium indicate that for $\theta_i < 60°$, the emissivity increases with roughness. For larger θ_i, the directional emissivity is less than for an ideal smooth surface; this is a result of both roughness and the behavior of ideal smooth metallic surfaces where the emissivity becomes large for directions nearly tangent to the surface. The roughness models are also used with ray tracing methods to simulate realistic visual reflection from objects (Wolff and Kurlander 1990). Jo et al. (2017) applied geometric optics to simulate the emissivity of oxidized steel, using a surface profile derived from a Fourier series.

Tang and Buckius (1999) reviewed literature on surface reflection (surface scattering) models and experiments. The influence of incidence angle, radiation wavelength, surface materials, and surface geometry on scattering from a surface is discussed. Both deterministic and probabilistic surface models are presented. It is noted that polarized energy incident on tailored 2D rough surfaces can provide extremely strong spikes in reflectivity, particularly when the wavelength of the incident radiation is such that resonance occurs within the surface cavities. Comparisons between predictions and measurements are in good agreement, adding confidence in the use of EM theory for these predictions.

A regime map is given by Dimenna and Buckius (1994a) to show the region of validity of the various approaches for predicting surface reflectivity of a highly conducting material with roughness that varies only in one direction. The exact solution of Maxwell equations is compared with a geometric optics solution using Fresnel reflection equations applied to the tangent plane of the surface roughness at each point of incidence, i.e. Kirchhoff's approximation.

Another regime map, shown in Figure 3.37, depicts when geometric optics provide a specified acceptable level of accuracy for one-dimensional (1D) roughness on a perfectly conducting surface (Tang et al. 1977). The axes on the plot are the surface rms roughness σ_0 over the roughness correlation length τ, Equation (3.42), versus the ratio of roughness times the cosine of the incidence angle divided by the wavelength, $\sigma_o \cos\theta_i/\lambda$. The shaded region is delineated by comparing the results of EM theory computations with geometric optics results for over 40 surfaces. The boundary is drawn where the error is less than 20%; outside of the shaded region, detailed analysis using EM theory is required. This map was derived for perfectly conducting surfaces; similar results for dielectric surfaces indicate that the region increases where geometric optics provides good agreement. For a given roughness, if the wavelength is small relative to the roughness, the geometric optics approximation applies. This is also true if the correlation length is large so that the roughness has a less random irregularity. A more recent regime map is provided by Fu and Hsu (2008). K. H. Lee (2019) uses an inverse technique to estimate emissivity distributions, and H. J. Lee (2019) uses geometric-optics-based Monte Carlo (Chapter 14) to determine the reflectivity distributions of rough silicon and aluminum surfaces with known Gaussian slope and height distributions, and then uses regression to fit relations for the reflectivity.

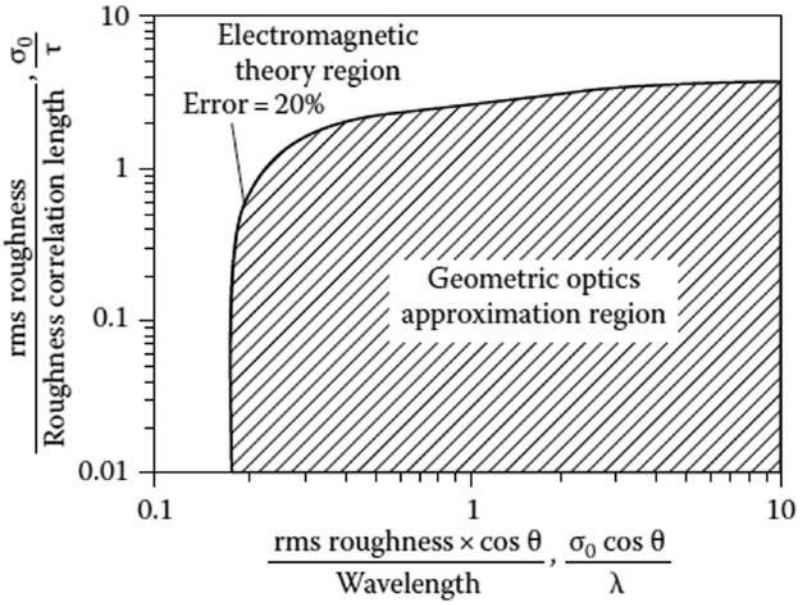

FIGURE 3.37 Region of validity (within 20% error) for using geometric optics analysis of reflectivity for rough surfaces. (From Tang, K. et al., *IJHMT*, 40, 49, 1977).

3.3.3 Variation of Radiative Properties with Surface Temperature

3.3.3.1 Non-metals

Theoretical predictions of the effect of temperature on the radiative properties of insulators are varied and complex. Figure 3.38 shows how the normal spectral emissivity of two ionic crystals, LiF and MgO, change with temperature. In general, the normal spectral emissivity increases at short wavelengths but drops at long wavelengths. Solid lines show fits obtained from Lorentz theory, Equation (3.38); Jasperse et al. (1966) explain these trends by interpreting how the resonant frequency, $\omega_{o,j}$, and the damping constant, ζ_j, may be affected by temperature. The radiative properties of amorphous materials tend to be insensitive to temperature, as shown in Figure 3.39 for a SiC material and sintered Al_2O_3. In cases in which the radiative properties of a ceramic are observed to change significantly with temperature, these changes may be due to temperature-induced changes in the surface structure or the formation of oxidation with heating.

In general the index of refraction for non-conductors is weakly dependent on temperature; consequently, ε_λ is insensitive to temperature, and variation of total emissivity with temperature is dominated by how the spectral shift in $E_{\lambda b}$ influences the relative weighting of ε_λ. This provides the very useful result that the ε_λ measured at one temperature can be used in the integral to calculate accurate ε values over a range of nearby temperatures. Figures 3.40 and 3.41 show the total normal and total emissivity for several ceramic materials. Both increasing and decreasing trends with temperature are observed.

3.3.3.2 Metals

In Section 3.2.2 it was shown that the normal spectral emissivity of metals tends to increase as wavelength decreases in the IR region. Figure 3.42 shows the spectral normal emissivity for several polished metals at high temperatures, and this generally holds in other directions as shown in Figure 3.6, except at large angles from the normal, where various spectral profiles may cross. At sufficiently long wavelengths $\lambda > \sim 5$ μm, Hagen–Rubens theory predicts that the normal spectral emissivity should be proportional to $\lambda^{-1/2}$, which is the case for the data from iron, platinum, nickel,

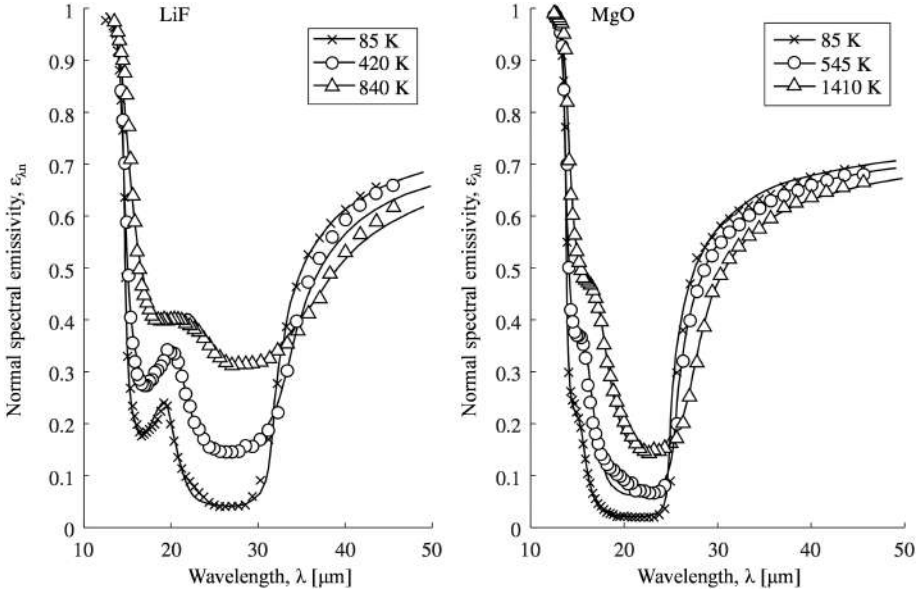

FIGURE 3.38 Effect of temperature on the normal spectral emissivity of LiF and MgO. Solid curves denote Lorentz theory, Equation (3.38). (From Jasperse, J. R., Kahan, A., Plendl, J. N.: Temperature dependence of infrared dispersion in ionic crystals LiF and MgO, *Phys. Rev.,* 146(2), 526, 1966).

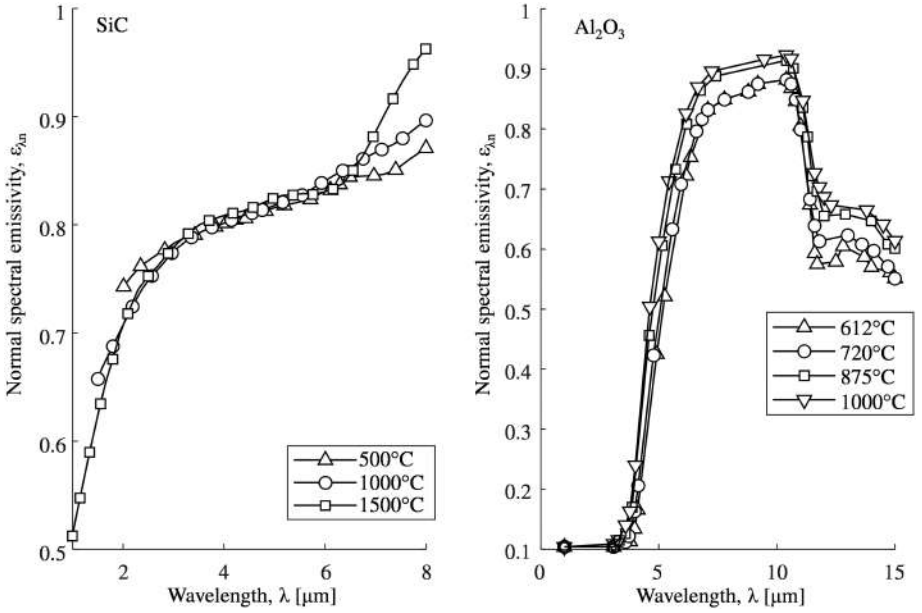

FIGURE 3.39 Normal spectral emissivity for various temperatures of a silicon carbide material, Hexoloy ST (as received) and sintered alumina. (SiC from Postlethwait, M.A. et al., *JTHT*, 8(3), 412, 1994: Al_2O_3 from Touloukian, Y.S. and Ho, C.Y. (eds.), Thermophysical Properties of Matter, TRPC Data Services; Volume 8, *Thermal Radiative Properties: Nonmetallic Solids, 1972*).

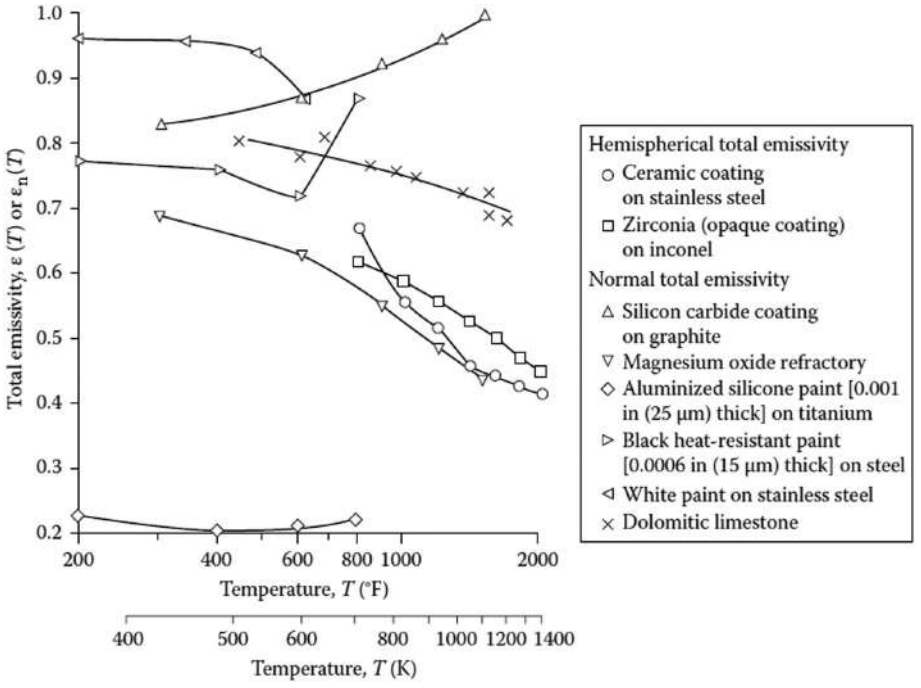

FIGURE 3.40 Effect of surface temperature on total emissivity of dielectrics. (From Touloukian, Y.S. and Ho, C.Y.: Thermophysical properties of matter, in Y.S. Touloukian and D.P. DeWitt (eds.), Volume 9, *Thermal Radiative Properties: Metallic Elements and Alloys*, 1970; and *Thermal Radiative Properties: Coatings*, 1972b; Grewal, N.S. and Kestoras, M., *IJHMT*, 31(1), 207, 1988).

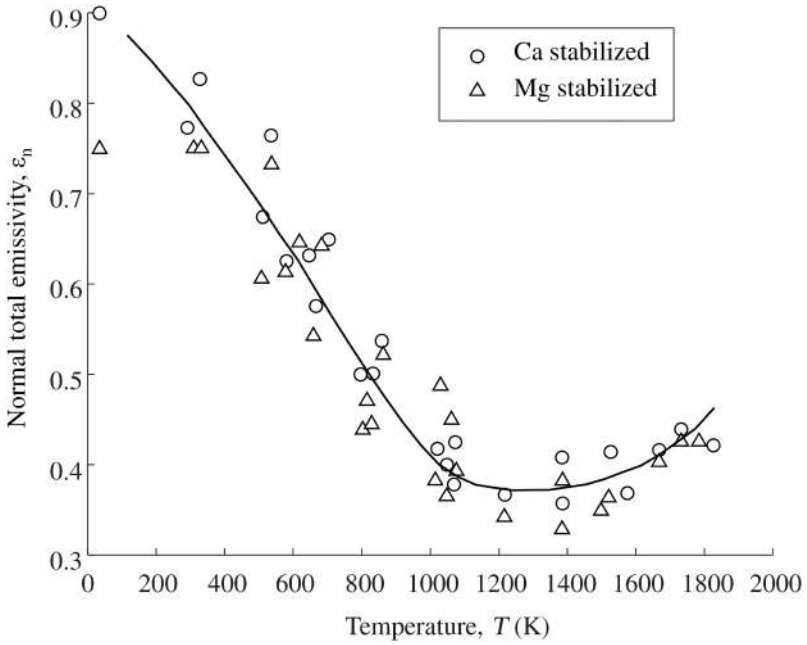

FIGURE 3.41 Effect of surface temperature on normal total emissivity of zirconium oxide. (From Wood, W.D. et al.: *Thermal Radiative Properties*, Plenum Press, New York, 1964.)

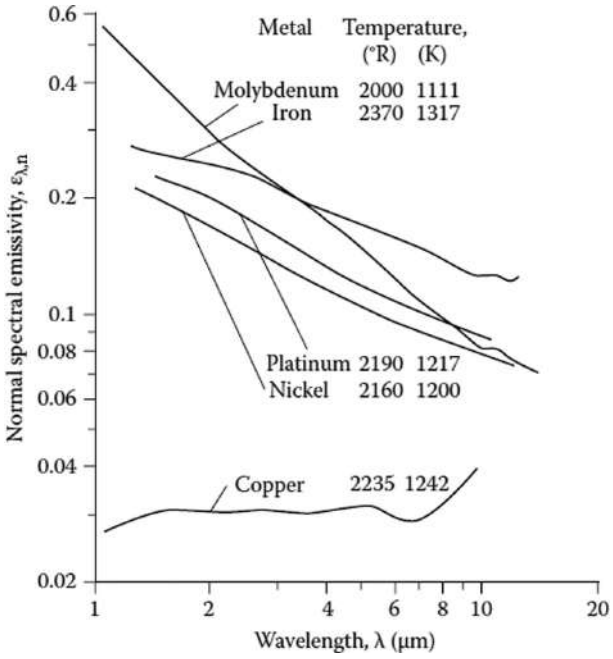

FIGURE 3.42 Variation with wavelength of normal spectral emissivity for polished metals. Dashed lines show $\varepsilon_{\lambda,n} \propto \lambda^{-1/2}$. (From Seban, R.A.: *Thermal Radiation Properties of Materials*, pt. III, WADD-TR-60–370, University of California, Berkeley, CA, August 1963).

and tungsten samples plotted in Figure 3.42. The curve for the copper sample illustrates an exception as the emissivity remains relatively constant with wavelength. As described in Section 3.2.3, at very short wavelengths, the assumptions underlying Hagen–Rubens theory become invalid. Most metals exhibit a peak emissivity somewhere near the visible region, and the emissivity decreases rapidly with further increases in wavelength.

Hagen–Rubens theory also predicts that the spectral emissivity of pure metals should increase with temperature, as its resistivity does, and this is usually found to be the case. Figure 3.43 is an example of the hemispherical-spectral emissivity of tungsten (De Vos 1954). The expected trend is observed for $\lambda > 1.27$ μm. In particular, since the Hagen–Rubens theory predicts that $\varepsilon_\lambda \propto r_e^{1/2}$ and the resistivity of many metals varies linearly with temperature, *cf.* Equation (3.33), it follows that ε_λ should also vary with the square root of temperature (in K). This should also approximately hold for hemispherical values, which is shown to be the case in Figure 3.43 at $\lambda = 2$ μm, although at this wavelength one may not expect an accurate quantitative prediction using Hagen–Rubens theory.

Figure 3.43 also illustrates a characteristic of many metals, as discussed by Sadykov (1965). At short wavelengths (in the case of tungsten, $\lambda > 1.27$ μm), the temperature effect is reversed and the spectral emissivity decreases with increased temperature. The emissivity curves all cross at the same point, called the "X point." Sell et al. (1964) provide a theoretical explanation of the X-point based on how the electron density-of-states varies with temperature. Other X points for different metals include iron, 1.0 μm; nickel, 1.5 μm; copper, 1.7 μm; and platinum, 0.7 μm. Thermionic energy conversion devices use high-temperature alloys of tungsten and rhenium compounded with thoria and hafnium carbide. Their normal spectral emittances were measured by Tsao et al. (1992), and results were given for temperatures from 1500 to 2500 K. Most of the results are at $\lambda = 0.535$ μm, and the normal spectral emittances were found to decrease linearly with increasing temperature. This is the expected trend, since the wavelength is smaller than at the X point and hence spectral emissivity should decreases as temperature increases.

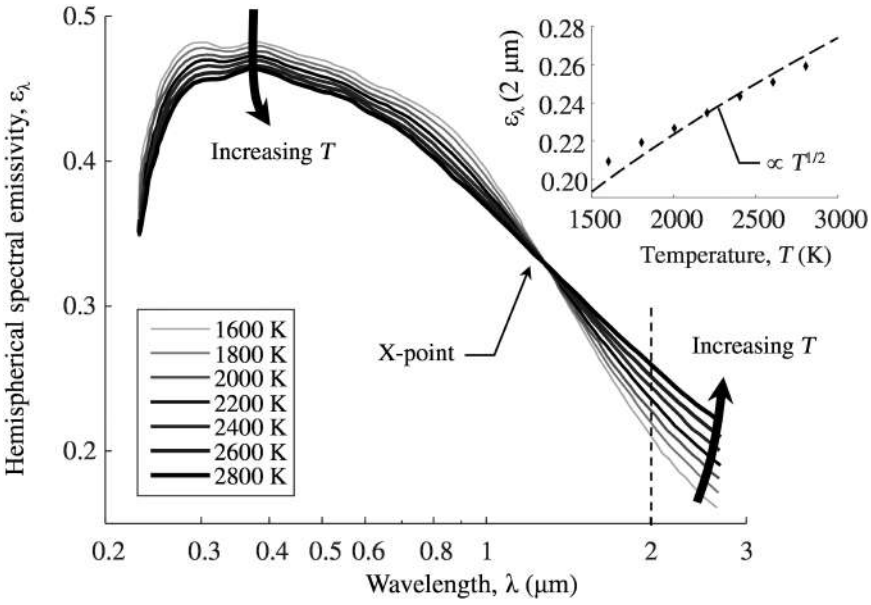

FIGURE 3.43 Effect of wavelength and surface temperature on hemispherical-spectral emissivity of tungsten. (From De Vos, J.C., *Physica*, 20, 690, 1954).

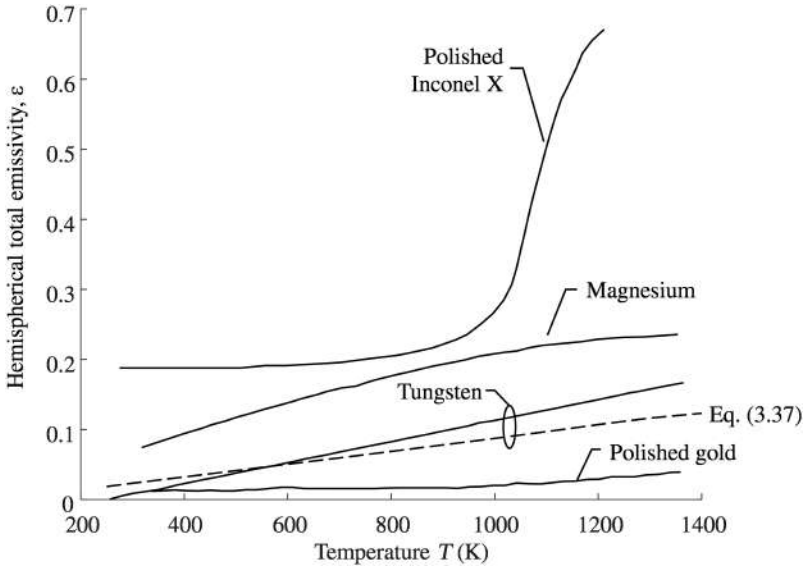

FIGURE 3.44 Effect of temperature on hemispherical total emissivity of several metals. (From Touloukian, Y.S. and Ho, C.Y. (eds.): *Thermophysical Properties of Matter*, TRPC Data Services; Volume 7, *Thermal Radiative Properties: Metallic Elements and Alloys*, Touloukian, Y.S. and DeWitt, D.P., 1970).

The increase of spectral emissivity with decreasing wavelength for metals in the IR region (wavelengths longer than in the visible region) accounts for the increase in total emissivity with temperature. With increasing temperature, the peak of the blackbody radiation distribution (Figure 1.10) moves toward shorter wavelengths. Consequently, as the surface temperature increases, proportionately more radiation is emitted in the region of higher spectral emissivity, which increases the total emissivity. Some examples are plotted in Figure 3.44; in the case of tungsten, experimental

measurements are compared with Equation (3.37), derived by Parker and Abbott (1964) from Hagen–Rubens theory.

The radiative properties of surfaces at extremely low temperatures provide key fundamental insights into the electronic structure of materials, and are also important in many practical engineering applications, for example, vacuum cryogenic insulation systems where the dominant heat transfer mechanism is through radiative transfer. Were electrical resistivity directly proportional to temperature, Hagen–Rubens theory would indicate that emissivities should become quite small at low T and large λ. Likewise, Drude theory, which reduces to Hagen–Rubens relation at long wavelengths, predicts ε values that decrease much more rapidly with temperature than has been observed. Experimental measurements summarized by Toscano and Cravalho (1976) for copper, silver, and gold indicate that ε does not decrease to such small values. The anomalous skin-effect model with diffuse electron reflections was found to predict the emissivity most accurately. Figure 3.45 shows results of the model. Similar results for gold films are reported by Tien and Cunnington (1973). Frolec et al. (2019) provide a database of measured total hemispherical absorptivity and emissivity data in the cryogenic range from 20 K to between 120 and 320 K for 58 polished metals, metal foils, and metals with various surface finishes. They show agreement with previous measurements, and also show the expected increases in emissivity when polished surfaces are abraded to various degrees.

It is fitting to conclude this section with two final remarks: First, while EM theory may predict how the emissivity of a metal surface varies with changes in wavelength and temperature, quantitative agreement between these values and experimental measurements should only be expected for polished specimens, and otherwise should be considered as a lower bound due to surface roughness.

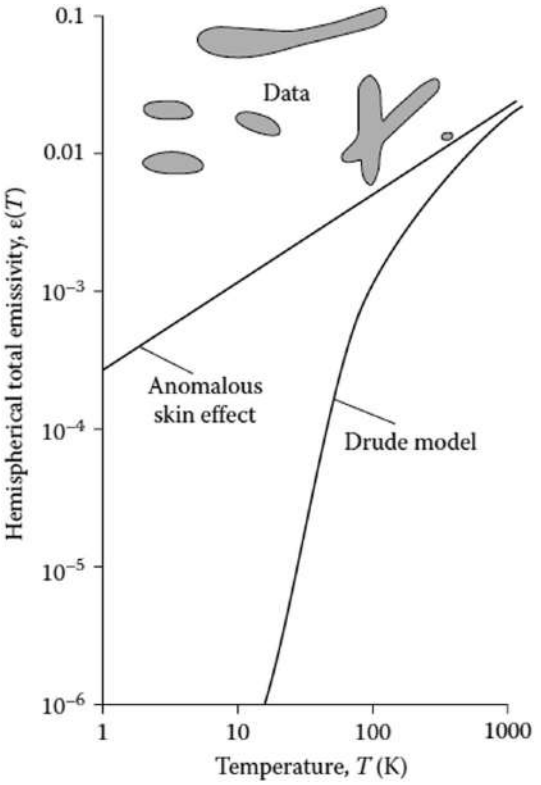

FIGURE 3.45 Effect of low temperatures on hemispherical total emissivity of copper. (Results from Toscano, W.M. and Cravalho, E.G., *JHT*, 98(3), 438, 1976).

Second, a temperature-induced change in surface morphology of a metal, e.g., oxidation, often has a far greater influence on the radiative properties than one would expect via Hagen–Rubens theory, again keeping in mind that this theory is limited to longer wavelengths.

3.3.4 Properties of Liquid Metals

Liquid metals tend to be more reflective compared to their solid counterparts, since their surface is perfectly smooth. Among numerous studies that have investigated the radiative properties of liquid metals, of particular note is a series of papers by Krishnan et al., who employed a containerless technique through magnetic levitation to avoid chemical reactions between the sample and gas or crucible that can occur at extreme temperatures. These studies include Krishnan et al. (1990a) (copper, silver, gold, nickel, palladium, platinum, and zirconium), Krishnan et al. (1990b), (liquid silicon, aluminum, titanium, and niobium), Krishnan and Nordine (1993) (aluminum), and Krishnan et al. (1997) (nickel and iron). A subset of these results is plotted in Figure 3.46, showing that $\varepsilon_{\lambda n}$ is nearly independent of temperature. Moscowitz et al. (1972) reported the spectral emissivity values at $\lambda = 0.645$ μm of three rare earth liquid metals, which were similarly independent of temperature. This can be attributed to the fact that in solid metals the electrical resistance increases with temperature largely due to temperature-induced lattice vibrations, which scatter the electrons, while liquid metals have no atomic lattice.

Figure 3.47 shows how the normal spectral reflectance of several liquid metals varies with respect to wavelength. Drude theory, discussed in Section 3.2.3, is often successful for liquid metals since the electronic band structure caused by the periodicity of the crystal lattice disappears upon melting, and in many cases the radiative properties at infrared wavelengths can be interpreted solely in terms of intraband electronic transitions involving conduction band electrons (Faber 1972). Several studies show very good agreement between the dielectric constants calculated from ellipsometry measurements on molten metal and those predicted from Drude theory using the published density and DC conductivity, e.g., Miller (1969) and Comins (1972). (See Figure 8.10).

In other cases where interband transitions are important, e.g., liquid iron and nickel (Krishnan et al. 1997), Drude theory cannot be applied. Havstad et al. (1993) reported the normal spectral emissivity of molten uranium, another transition metal, between 0.4–10 μm and at temperatures

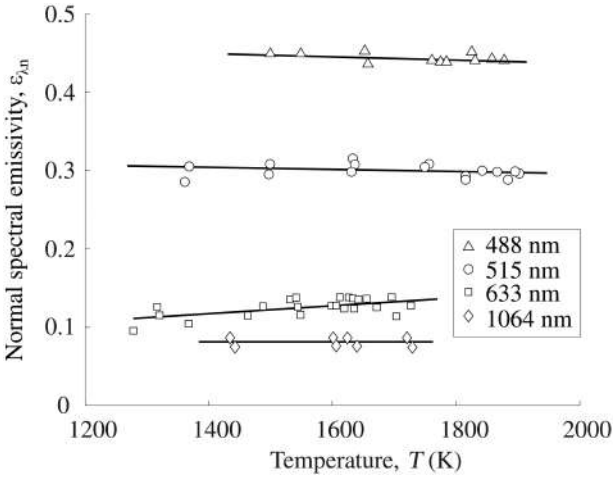

FIGURE 3.46 Normal spectral emissivity of molten copper as a function of temperature at four different wavelengths. From Krishnan, S., Hansen, G. P., Hauge, R. H., Margrave, J. L.: Emissivities and optical constants of electromagnetically levitated liquid metals as functions of temperature and wavelength, In *Materials Chemistry at High Temperatures*: Volume 1 Characterization, J. W. Hastie (ed), Springer, 1990.

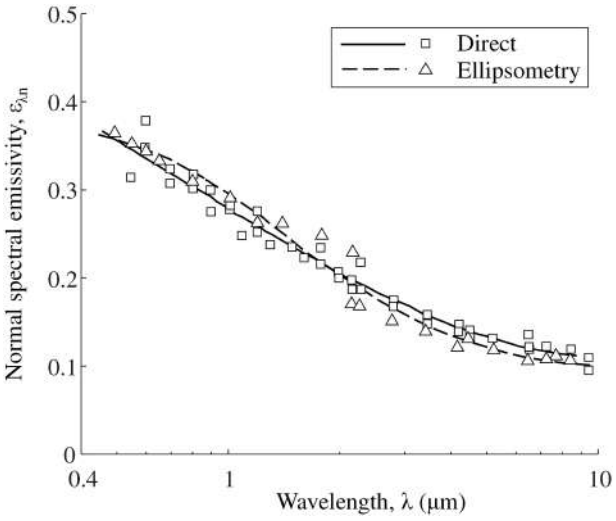

FIGURE 3.47 Normal spectral emissivity of liquid uranium between 1410 K and 1630 K. (From Havstad, M.A. et al., *JHT*, 115, 1013, 1993).

between 1410–1630 K. Both direct emittance and ellipsometry measurements were carried out. At longer wavelengths $\varepsilon_{\lambda n}$ is found to diminish with respect to wavelength, as shown in Figure 3.47. This is consistent with the general trend expected from Hagen–Rubens theory, although the refractive index inferred from ellipsometry could not be reproduced using Equation (3.26) due to interband transitions that are unaccounted for in this model.

Havstad and Qiu (1996) used the electrical resistivity and Hall coefficients for liquid metals to predict the spectral normal emissivity of liquid cerium/copper alloys. Agreement with published data is good, and extension to copper-, gold-, silver-, and aluminum-rare Earth alloys is also expected to be good from similarities in property behavior for these alloys (important in laser-cladding technologies).

3.3.5 Properties of Semiconductors and Superconductors

Semiconductors are a particularly important case since the spectral emissivity must be known in order to measure the temperature of silicon wafers during rapid thermal processing. When the photon energy is greater than the band gap energy of silicon (~1.14 eV, or ~1.09 μm) the radiative properties are dominated by electron transitions between the valence and conduction bands. At longer wavelengths, however, the EM field interacts primarily with free carriers in the valence band (holes) and the conduction band (electrons).

Semiconductors are often "doped" with impurities to tune their electronic properties, and, as one may expect, this has a pronounced effect on the radiative properties as shown in Figure 3.48 for silicon. Radiative properties depend both on the carrier density (holes and electrons) as well as the scattering, which is dominated by the presence of impurities. Several researchers have attempted to model how doping may influence the radiative property through a modified Drude theory that accounts for both holes and electrons (e.g., Basu et al. 2010.) Liebert and Thomas (1967) demonstrated that the radiative properties of doped silicon could be modeled as that of a metal with high resistivity using the Hagen–Rubens relations.

While silicon and germanium are semiconductors in solid state, in liquid form they are metals because the valence band electrons that are localized by covalent bonds are released and form a conduction band upon melting. Consequently, liquid silicon and germanium have a high normal reflectance in the visible wavelengths, in contrast to the solid state (Lampert et al. 1981), as shown

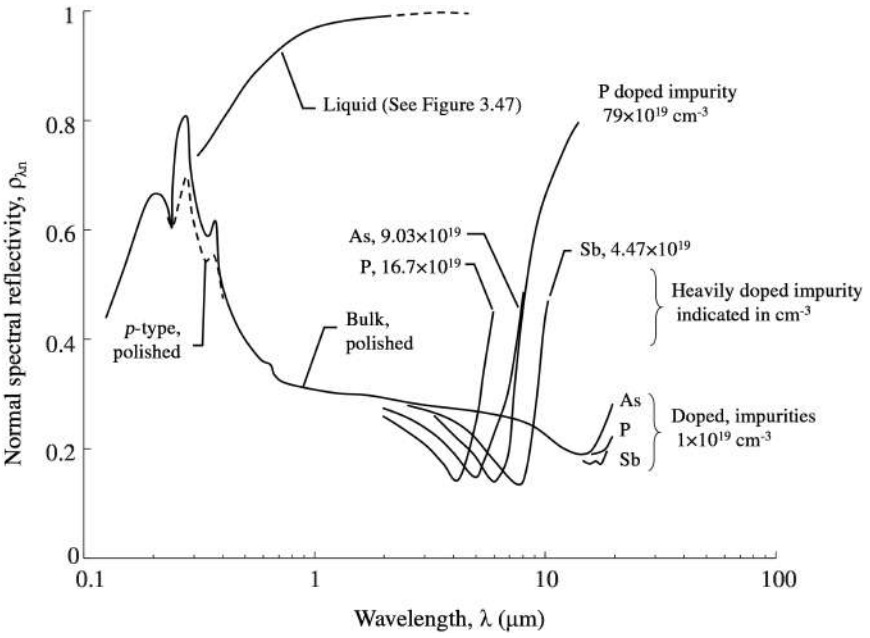

FIGURE 3.48 Spectral normal reflectance of pure and doped silicon. (Adapted from Touloukian, Y.S. and Ho, C.Y. (eds.), Thermophysical Properties of Matter, TRPC Data Services; Volume 8, *Thermal Radiative Properties: Nonmetals*).

in Figure 3.49. A number of Drude models for liquid Si and Ge have been derived either by fitting $\omega_{p,}$ and ζ from Equation (3.39) to ellipsometry measurements or from the density and DC resistivity of the molten semiconductor, as described in Chapter 8 (Shvarev et al. 1977, Li and Fauchet 1987, Jellison and Lowndes 1987, Kawamura et al. 2005).

3.4 SELECTIVE SURFACES FOR SOLAR APPLICATIONS

It is often desirable to tailor the radiative properties of surfaces to increase or decrease their natural ability to absorb, emit, or reflect radiant energy. This is particularly the case in solar-related applications: In some instances the goal is to maximize the fraction of solar energy absorbed at short wavelengths and minimize emission losses at longer wavelengths, e.g., solar collectors, while in other cases the fraction of reflected sunlight should be maximized to reduce the cooling load of buildings in the summer. (This is often called "radiative cooling.") While so-called spectrally selective surfaces have long been used for these purposes, recent advancements in nanotechnology allow engineers to precisely "tune" surface properties according to the requirements of the specific application, leading to significant performance improvements. To understand the performance of these types of surfaces, we first review the key characteristics of solar radiation.

3.4.1 Characteristics of Solar Radiation

The key attributes that describe solar irradiation are the solar constant and the solar temperature. The solar constant describes the average total solar irradiation incident on a surface normal to the sun at a distance equal to the Earth's mean radius from the sun; it accounts for the solid angle subtended by the sun as viewed by the earth, but excludes attenuation of solar energy by the atmosphere. The accepted value by many standards organizations including the American Society for Standards and Measurement (ASTM) is 1366 W/m^2, although the National Oceanographic and Atmospheric

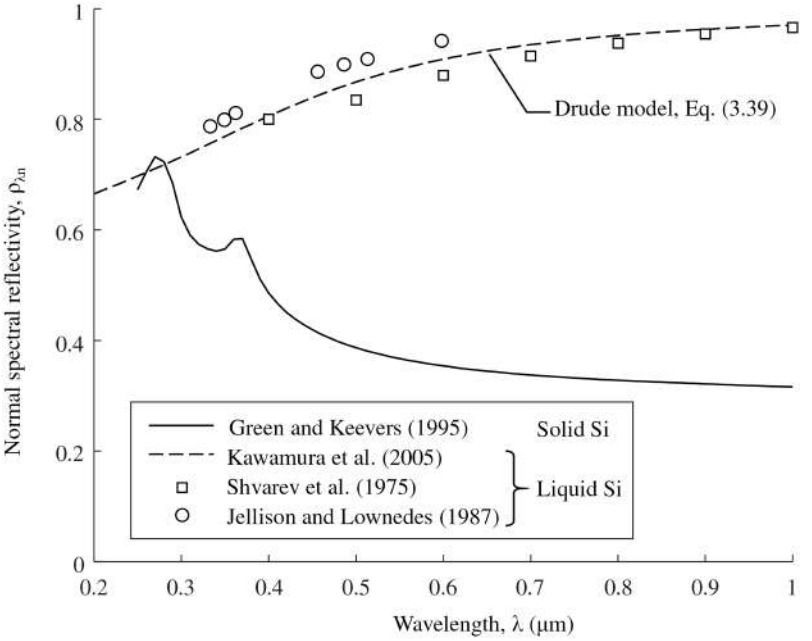

FIGURE 3.49 Spectral normal reflectance of polished solid and liquid silicon. Solid silicon data is from Green and Keevers (1995). Liquid silicon measurements are from Shvarev et al. (1975) and Jellison and Lowndes (1987); Drude model is from Kawamura et al. (2005).

Administration (NOAA) uses a value of 1376 W/m^2. The value fluctuates slightly with time due to changes in the solar energy output. Larger changes are due to the eccentricity of the earth's orbit about the sun, causing variations from 1322 W/m^2 at aphelion to 1412 W/m^2 at perihelion. In this book we use a value of 1366 W/m^2 unless specified otherwise.

The solar temperature defines the spectral distribution of solar irradiation, which is close to that of a blackbody at a temperature of 5780 K. The radiation reaching the earth's surface comes from the plasma contained in the sun's photosphere and originates from *bremsstrahlung* radiation ("braking radiation") emitted as excited electrons in the plasma decelerate around the ions and neutrals. The photosphere has a much lower temperature than the sun's interior (millions of degrees) where a thermonuclear reaction is occurring.

3.4.2 Modification of Surface Spectral Characteristics

For surfaces that collect solar energy, such as in solar distillation units, solar furnaces, or solar collectors for energy conversion, it is desirable to maximize the energy absorbed while minimizing emission losses. In solar thermionic or thermoelectric devices, the best performance is obtained by maintaining the solar-irradiated surface at its highest possible equilibrium temperature. For photovoltaic (PV) solar cells, absorption should be maximized within the bandgap of the PV material to maximize electrical output, but absorption should be minimized in the IR spectrum to minimize heating of the cells and minimize cooling requirements (Hajimirza et al. 2011, 2012, Hajimirza and Howell 2012, 2013a, b, 2014a, b.). For situations where a surface is to be kept cool while exposed to the sun, it is desired to have maximum reflection of solar energy with maximum radiative emission from the surface.

For solar energy collection, a black surface maximizes the absorption of incident solar energy; unfortunately, it also maximizes the emissive losses. However, if a surface could be manufactured

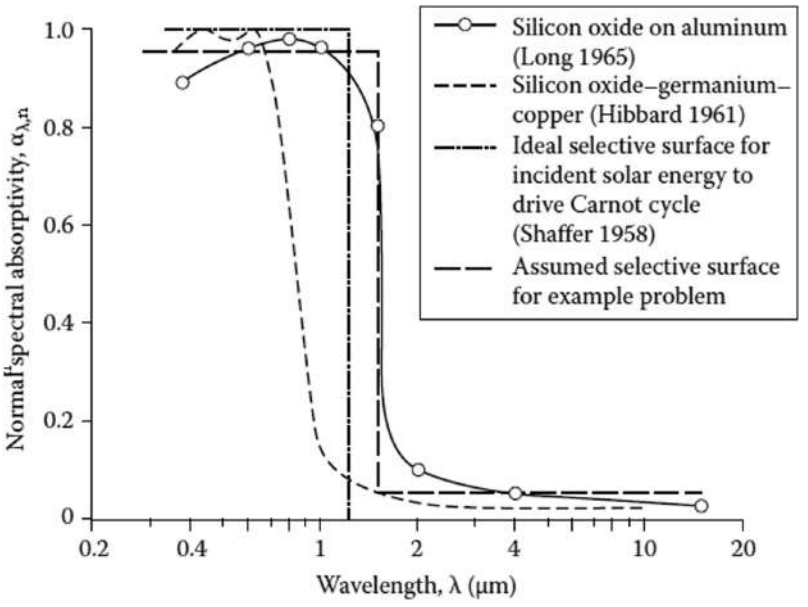

FIGURE 3.50 Characteristics of some spectrally selective surfaces.

that had a large absorptivity in the spectral region of short wavelengths about the peak solar energy, yet small in the spectral region of longer wavelengths where the peak surface emission would occur, it might be possible to absorb nearly as well as a blackbody while emitting very little energy. Such surfaces are called "spectrally selective." One method of manufacture is to coat a thin, nonmetallic layer onto a polished metallic substrate. As discussed in Section 3.3.1, the thin coating is essentially transparent at long wavelengths, and the surface is highly reflective due to the substrate metal. At short wavelengths, however, the radiation characteristics approach those of the nonmetallic coating, so the spectral emissivity and absorptivity are relatively large. Some examples of this behavior are in Figure 3.50 (Shaffer 1958, Hibbard 1961, Long 1965).

An ideal solar-selective surface maximizes the amount of absorbed solar irradiation while minimizing losses due to emission. A good surface should therefore have a spectral absorptivity near unity over short wavelengths where the incident solar energy has a large intensity and a low spectral emissivity close to zero at longer wavelengths. The wavelength at which this transition occurs, as shown in Figure 3.50, is the *cutoff wavelength*.

A performance parameter for a solar-selective surface is the ratio of its directional total absorptivity $\alpha(\theta_i, \phi_i, T)$ for incident solar energy to its hemispherical total emissivity $\varepsilon(T)$. The ratio $\alpha(\theta_i, \phi_i, T)/\varepsilon(T)$ for the condition of incident solar energy is a measure of the theoretical maximum temperature that an otherwise insulated surface can attain when exposed to solar radiation. In general, the energy absorbed per unit time by a surface element dA

where I_{solar} is the incident (total) solar intensity, $d\Omega_{solar}$ is the solid angle subtended by the sun as viewed by dA, and G_{solar} is the corresponding directional energy flux. The total energy emitted per unit time by the surface element is

If there are no other modes of energy transfer (e.g., conduction or convection losses), the emitted and absorbed energies are equated to give

where T_{eq} is the equilibrium temperature that is achieved. Thus, the ratio $\alpha(\theta_i,\phi_i,T)/\varepsilon(T)$ for $T \approx T_{eq}$ is a measure of the equilibrium temperature of the element. Note that the temperature at which the properties α and ε are selected should be the equilibrium temperature that the body attains.

For the collection and utilization of solar energy on Earth or in outer space applications, it is common to have normal solar incidence so that $\alpha = \alpha_n$ and $\cos\theta_i = 1$. Naturally, a high α_n/ε is desired. For the relatively low temperatures of solar collection in ground-based systems without solar concentrators, selective paints on an aluminum substrate have $\alpha_n = 0.92$ and $\varepsilon = 0.10$ (Moore 1985). Low-emittance metallic flakes also mixed in a binder with high-absorptance metallic oxides to yield coatings with $\alpha_n = 0.88$ and $\varepsilon = 0.40$. For ground-based solar collectors, convection heat transfer must be included in the energy balances, and solar collectors are often designed to minimize these losses. To attain high equilibrium temperatures for space power systems, polished metals attain α_n/ε of 5–7, and specially manufactured surfaces have α_n/ε approaching 20. Coatings with $\alpha_n/\varepsilon \approx 13$ and stability at temperatures up to about 900 K in air are reported by Craighead et al. (1979). Space power systems usually have a concentrator such as a parabolic mirror. This increases the collection area relative to the area for emission and thus effectively increases the absorption-to-emission ratio even further. Economical and durable paints are desired for application to large solar collection areas. Many of these ideas are discussed in reviews by Granqvist (2003) and Wijewardane and Goswami (2012).

The energy equation solved in Example 3.6 is a two-spectral-band approximation to the following more general energy-balance equation for a *diffuse* surface:

The $G_{\lambda,\text{solar}}d\lambda$ can have any spectral distribution, and by Kirchhoff's law $\alpha_\lambda(T_{eq}) = \varepsilon_\lambda(T_{eq})$ for a diffuse surface. A more general situation is in Figure 3.51, where the absorption of incident energy from the θ_i direction depends on the directional-spectral absorptivity $\alpha_\lambda(\theta_i,\phi_i,T_{eq})$. The emission from the surface depends on its hemispherical-spectral emissivity $\varepsilon_\lambda(T_{eq})$. The q_e is the heat flux supplied to the surface by any other means, such as convection, electrical heating, or radiation to its lower side. The heat balance then becomes

Equation (3.47) is readily solved by using integration subroutines and root solvers. This analysis can be used for temperature control of space vehicles, as shown by Furukawa (1992), who determined the solar and Earth radiation fluxes incident on the different surfaces of an orbiting vehicle.

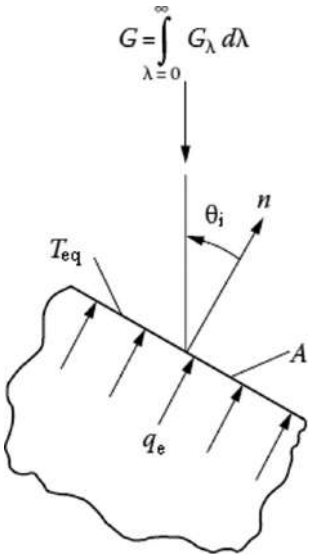

FIGURE 3.51 Radiative energy incident on a selective surface.

Spectrally selective surfaces can also be useful where it is desirable to cool an object exposed to incident radiation from a high-temperature source. Common situations are objects exposed to the sun, such as a hydrocarbon storage tank, a cryogenic fuel tank in space, or the roof of a building. Equation (3.46) shows that the smaller the value of α/ε that can be reached, the lower will be the equilibrium temperature. For a cryogenic storage tank exposed to solar flux in the vacuum of outer space, α_n/ε should be as small as possible in order to reduce losses by heating the stored cryogen. In practice, values of $\alpha(\theta_i)/\varepsilon$ in the range 0.20–0.25 can be obtained for normal incidence ($\cos\theta_i = 1$). A highly reflecting coating such as a polished metal can also be used for some applications. This would reflect much of the incident energy but would be poor for radiating away energy that was absorbed or generated within an enclosure, such as by electronic equipment. This behavior is important for the energy balance in the vacuum of outer space and may not provide a low α/ε, but this may not be important when there is appreciable convective cooling that dominates over radiant emission. Some metals may not work well because they have a tendency toward lower reflectivity at the shorter-wavelengths characteristic of the incident solar energy, e.g., aluminum. For some applications, spectrally selective materials are used. As discussed in Section 3.3.1, white paint is another example of spectrally selective surface.

For thermal control in outer space, different spectrally selective surfaces have been defined. Among them, the optical solar reflector (OSR) is a mirror composed of a glass layer silvered on the back side. The glass, being transparent in the short-wavelength region, $\lambda < \sim 2.5$ μm, which includes the visible range, lets the silver reflect incident radiation in this spectral region. The small fraction of short-wavelength energy that is absorbed by the silver and the energy absorbed by the glass at longer wavelengths are radiated away by the glass in the longer-wavelength IR region where glass emits well. Commonly used thin plastic sheets for solar reflection are Kapton, Mylar, and Teflon with silver or aluminum coated on the back side. The long-term radiative performance of these materials

after ten years' exposure in geosynchronous orbit is evaluated by Hall and Fote (1992). Fused-silica second-surface mirrors and polished metals are essentially stable in orbit. Metalized Teflon, aluminized Kapton, and some light-colored paints, on the other hand, darken over a long period of time, degrading their performance (Hall and Fote).

Radiative dissipation is vital in outer space applications, as there is no other means to eliminate waste energy except to dissipate small quantities by using expendable coolants. For a device on the ground or in the earth's atmosphere, convection and conduction to the surrounding environment are available. The significance of each of the three heat transfer modes depends on the particular conditions in the energy balance. An interesting example of such an energy balance is discussed by Berdahl et al. (1983) to show that radiative cooling might be useful for cooling buildings to help with air conditioning. Objects exposed to the night sky can cool by radiation to achieve temperatures below the ambient air temperature. This cooling effect can also be utilized during the day if the solar reflectivity of a surface is high (greater than about 0.95) and its emissivity is large in the IR. For this purpose, titanium dioxide white paint is somewhat superior, as an external solar-selective coating, to polyvinyl fluoride film with an aluminized coating 12 μm thick on the underside. These are the same types of materials, as well as many others that are used for spacecraft thermal control. The properties of these types of material are listed by Henninger (1984). The use of surface nanostructures to tailor spectral properties is discussed in Chapter 16.

There is also interest in developing selective emitters that emit most of their energy in a narrow spectral region rather than over a broad spectrum as for a blackbody emission. In a thermophotovoltaic converter, the absorbed radiant energy is converted into electrical energy. The conversion is possible only for energy within a small wavelength range. Hence, it is desired to irradiate the converter from a high-temperature surface that radiates primarily in the spectral region that provides effective electrical conversion. This provides good efficiency in the use of the radiated energy and hence efficient utilization of the energy used to heat the radiating surface such as a nuclear power source for applications in outer space. The fabrication of selective emitters by using rare Earth oxides is discussed by Rose et al. (1996). Another approach is discussed by Sentenac and Greffet (1994), where the theory is provided for designing a regular microroughness (a "grating") that will provide selective emission. The roughness dimension is of the same size range as the radiation wavelengths. An examination of performance, using EM scattering theory, indicates that wavelength-selective behavior can be obtained, which has been experimentally verified (Greffet and Henkel 2007). A near-blackbody absorber is reported by Zhao et al. (2019) through using a stacked microstructure comprised of a curved periodic stack of tungsten (15 nm) and polymethylpentene (TPX).

An extended discussion of spectrally selective surfaces for radiative cooling, along with recent references, is in the online Appendix J at www.ThermalRadiation.net. Optimization of nanogeometries for desired spectral-directional properties is discussed in Chapter 18.

3.4.3 Modification of Surface Directional Characteristics

As discussed previously, surface roughness can have profound effects on radiative properties and can become a controlling factor when roughness is large compared with the radiation wavelength. This leads to the concept of controlling surface texture to tailor the directional characteristics of a surface. A surface used as an emitter might be designed to emit strongly in preferred directions, while reducing emission into unwanted directions. Commercial radiant area-heating equipment would operate more efficiently by using such surfaces to direct energy where it is most needed. If the directional surface is primarily an absorber, then, using a solar absorber as an example, it should be strongly absorbing in the direction of incident solar radiation but poorly absorbing in other directions. The surface would, because of Kirchhoff's law for directional properties, emit strongly toward the sun but weakly in other directions. Such a surface then would absorb the same energy as a nondirectional absorber but would emit less than a surface that emits well into all directions.

The characteristics of one such surface are shown in Figure 3.52. The surface contains long parallel grooves with an open angle of 18.2° (Perlmutter and Howell 1963, Brandenberg and Clausen 1965). Each groove is coated with a highly reflecting specular material on the side walls, and a black surface is at the base. The solid line gives the behavior predicted by analysis of such an ideal surface, while the data points show experimental results at $\lambda = 8$ μm for an actual surface. The directional emissivity is very high for θ less than about 30° and decreases rapidly as the angle becomes large. Other such surface configurations exhibit similar characteristics; results for various V-, rectangular, and other grooves are also reported by Demont et al. (1982) and Mulford et al. (2018a, 2018b). EM wave theory was used by Ford et al. (1995) and Cohn et al. (1997) to predict the bidirectional-spectral reflectivity from surfaces with regular microcontours. The microcontour scales for the sinusoidal, rectangular, and V-grooves considered are on the order of the wavelength of the incident radiation so that geometric optics are not expected to apply. The theory and measurements are found to be in quite good agreement. The reflectivity of a V-groove is shown in Figure 3.53.

Surfaces with tailored roughness at the submicron scale can produce directional emissivity with extreme directionality (see, e.g., Figures 16.8 and 16.9) (Greffet et al. 2002, Greffet and Henkel 2007), and the theory behind these near-field effects is provided in Chapter 16.

3.5 CONCLUDING REMARKS

The radiative property examples in this chapter have illustrated features that may be encountered when dealing with real surfaces. Based on these data, we can make some useful generalizations, such as that the total emissivities of dielectrics at moderate temperatures are larger than those for metals and the spectral emissivity of metals increases with temperature over a broad range of wavelengths. However, these generalizations can be misleading because of the large property variations that may occur as a result of surface roughness, contamination, oxide coating, grain structure, and so forth. It is usually not possible to predict accurate radiative property values except for surfaces that approach ideal conditions of composition and finish. By coupling analytical trends with observations of experimental trends, it is possible to gain insight into what classes of surfaces would be expected to be suitable for specific applications and how surfaces may be fabricated to obtain

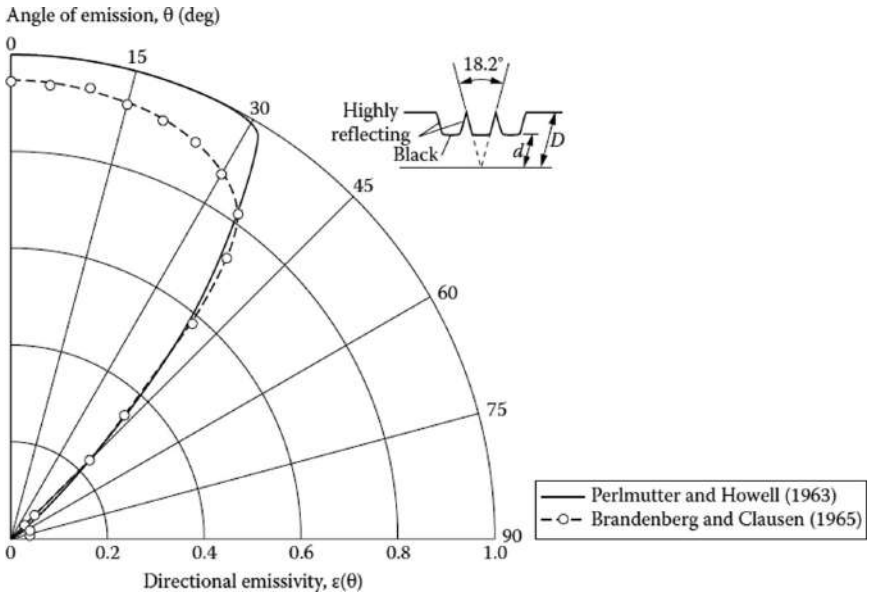

FIGURE 3.52 Directional emissivity of grooved surface with highly reflecting specular side walls and highly absorbing base; $d/D = 0.649$. Results in plane perpendicular to groove direction; data at $\lambda = 8$ μm.

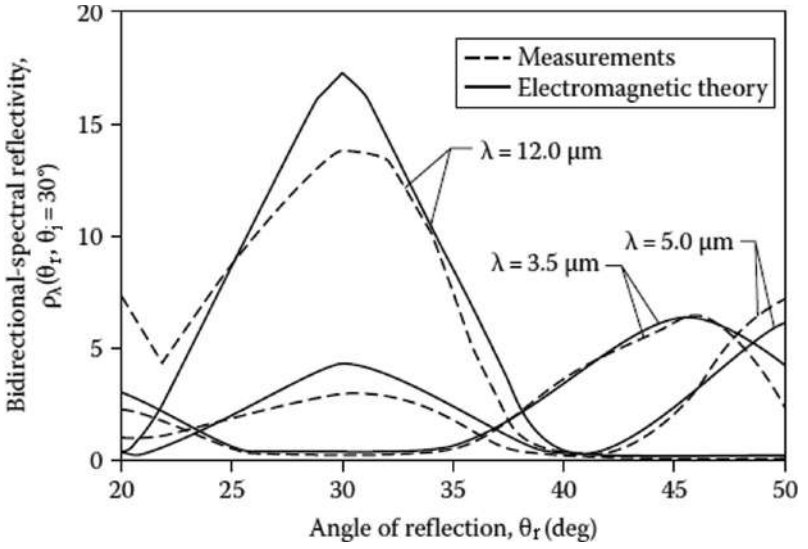

FIGURE 3.53 Bidirectional-spectral reflectivity in plane of incidence for a nickel V-groove cavity; width of cavity opening = 16.7 μm, cavity depth = 1.38 μm, angle of incidence θi = 30°. (From Cohn, D.W. et al., *IJHMT*, 40(13), 3223, 1997).

certain types of radiative behavior. The latter includes spectrally selective surfaces that are of great value in practical applications such as the collection of solar energy and spacecraft temperature control.

Finally, because of the growing interest in solar energy and the development of novel nanopatterning techniques, new designer materials for various applications are likely to surface. Similarly, traditional building materials, such as roof tiles, paints, facades, and windows, can be spectrally optimized to decrease the energy load on the buildings. The spectral emissivity could be designed to provide surfaces that strongly emit during the nighttime to optimize cooling of structures in hot climates (Rephaeli et al. 2013). The developments in spectral radiative transfer analyses may help to develop a wider database for spectral and directional radiative properties of different materials.